UNIVERSITY OF CALIFORNIA,
IRVINE

Unveiling Trends in Hydroclimate Extremes using High-spatiotemporal Resolution Climate Data Records of Precipitation

DISSERTATION

submitted in partial satisfaction of the requirements
for the degree of

DOCTOR OF PHILOSOPHY

in Civil and Environmental Engineering

by

Eric J. Shearer

Dissertation Committee:
Distinguished Professor Soroosh Sorooshian, Co-chair
Associate Adjunct Professor Phu Nguyen, Co-chair
Professor Amir AghaKouchak
Professor Kuo-lin Hsu

2022

Dedication

To my parents and sister

for their unwavering love, devotion, and support

Table of Contents

List of Figures

Page

List of Tables

Acknowledgements

The last five years of my life were an unexpected yet wonderful adventure that would not have been possible without the guidance, support, and love of the many people who've stuck by my side. First and foremost, I have to thank my family, especially my parents Richard and Iris, who raised me in a household of love and support, encouraged creativity, curiosity, independence, and openness, and stressed the value of education. I also would like to thank my sister Christine for blazing the Ph.D. trail—some might say that my decision to pursue a Ph.D. was the result of a sibling rivalry that got out of hand—yet she remained unflinchingly supportive from day one. I would also like to thank my sister-in-law Regiane for blessing our family with her light. I would also like to thank my extended family who've added richness to my life. Last but certainly not least, I would like to thank my wonderful partner Lilian, who stuck by my side for all five years of my program—through my highs and lows and from outside the country to cohabitating the same tiny room in my parent's house.

I would surely like to thank my co-advisors, Professor Phu Nguyen and Professor Soroosh Sorooshian, the former of whom took time every day to transform me from a callow young adult to a competent and hardworking professional, and the latter who taught me the poise, tact, and shrewdness of a true master. I surely would not have pursued a Ph.D. without their encouragement. I would also like to thank Professor Amir AghaKouchak for his guidance that led me to pursue my master's degree at UCI and my Ph.D. at the Center for Hydrometeorology and Remote Sensing. I would like to thank Professor Kuo-lin Hsu for his sharp intellect and keen eye, both of which were invaluable resources he happily shared with me as I pursued my projects. Lastly, I would like to thank my CHRS colleagues past and present for providing me with a network of support that helped smooth my transition into an entirely new field. I would also like to extend a thank you to the members of the atmospheric river community who have helped me along the way, especially the scientists of ARTMIP. I would like to acknowledge Scott Sellars who was a valuable mentor for me for my inquiries into atmospheric rivers and Brian Kawzenuk who provided me with intensive technical and data support for those works.

I am deeply grateful to the friends I've made along the way at UCI, who filled many roles in my life from supportive colleagues to Friday night pub buddies. I would especially like to thank the members of CEEGA past and present: Ari, Jawad, Lu, Matin, Sam, Sarah, and Vesta. My time at CEEGA was the most meaningful in my graduate career and every friend I made from there was among my closest. I would be remiss to not thank Ai-ling, Charlotte, Claudia, Danny, Debora, Matt, Megan, and Tim for their years of friendship. Outside of UCI, I must thank the friends who've stuck with me since public school and college for providing me a respite from graduate life.

I would like to acknowledge the American Geophysical Union for the copyright to Chapter 3. Atmospheric river catalogs produced for Chapter 3 are archived and available at the UC San Diego Library's Research Data Curation Program (https://doi.org/10.6075/J0D21W00), to whom we extend our sincerest thanks.

This work was partially supported by the Ridge to Reef NSF Research Traineeship (#DGE-1735040), Department of Energy (#DE-IA0000018), California Energy Commission (#300-15-005), the National Oceanic and Atmospheric Administration (#ST133017CQ0058) with Riverside

Technology, Inc., University of California (#4600010378 TO#15 Am 22), Center for Western Weather and Water Extremes (CW3E) at the Scripps Institution of Oceanography via AR Program Phase II (#4600013361) sponsored by CA-DWR, and UK Research and Innovation Global Challenges Research Fund Living Deltas Hub Grant (#NES0089261).

Vita

Eric J. Shearer

EDUCATION

2022 University of California, Irvine
Ph.D. in Civil and Environmental Engineering

2018 University of California, Irvine
M.S. in Civil Engineering

2016 University of California, Santa Barbara
B.S. in Earth Science
Minor in Astronomy and Planetary Science

PROFESSIONAL EXPERIENCE

2017–2022 Graduate Student Researcher
Center for Hydrometeorology and Remote Sensing, UC Irvine, Irvine, CA

2019 Summer Research Intern
NASA Earth Exchange, NASA Ames Research Center, Moffett Field, CA

2013–2015 Undergraduate Research Assistant
Experimental Cosmology Group, UC Santa Barbara, Santa Barbara, CA

PUBLICATIONS

1. Shearer, E.J., Nguyen, P., Gorooh, V.A., Hsu, K.L., Sorooshian, S., 2022. Unveiling Four Decades of Increasing Precipitation from Tropical Cyclones Using Satellite Measurements. *In production* in Scientific Reports.

2. Gorooh, V.A., Shearer, E.J., Nguyen, P., Hsu, K.L., Sorooshian, S., Cannon, F., Ralph, F.M, 2022. Performance of New Near-Real-Time PERSIANN Product (PDIR-Now) for Atmospheric River Events over the Russian River Basin, California. *In review* in Journal of Hydrometeorology.

3. Collow, A.B., Shields, C.A., Guan, B., Kim, S., Lora, J.M., McClenny, E.E., Nardi, K., Payne, A., Reid, K., Shearer, E.J., Tomé, Wille, J.D., Ramos, A.M., Gorodetskaya, I.V., Leung, L.R., O'Brien, T.A., Ralph, F.M., Rutz, J., Ullrich, P.A., Wehner, M., 2022. An Overview of ARTMIP's Tier 2 Reanalysis Intercomparison: Uncertainty in the Detection of Atmospheric Rivers and their Associated Precipitation. Journal of Geophysical Research: Atmospheres 127, e2021JD036155R. doi: 10.1029/2021JD036155

4. O'Brien, T.A., Wehner, M.F., Payne, A.E., Shields, C.A., Rutz, J.J., Leung, L.R., Ralph, F.M., Marquardt Collow, A.B., Guan, B., Lora, J.M., McClenny, E., Nardi, K.M., Ramos, A.M., Tomé, R., Sarangi, C., Shearer, E.J., Ullrich, P., Zarzycki, C.M., Loring, B., Huang, H., Inda Díaz, H.A., Rhoades, A.M., Zhou, Y., 2021. Increases in Future AR Count and Size: Overview of the

ARTMIP Tier 2 CMIP5/6 Experiment. Journal of Geophysical Research: Atmospheres 126, e2021JD036013. doi: 10.1029/2021JD036013

5. Sadeghi, M., Shearer, E.J., Mosaffa, H., Gorooh, V.A., Naeini, M.R., Hayatbini, N., Katiraie-Boroujerdy, P., Analui, B., Nguyen, P., Sorooshian, S., 2021. Application of Remote Sensing Precipitation Data and the CONNECT algorithm to Investigate Spatiotemporal Variations of Heavy Precipitation: Case Study of Major Floods Across Iran (Spring 2019). Journal of Hydrology, 126569. doi: 10.1016/j.jhydrol.2021.126569

6. Nguyen, P., Ombadi, M., Gorooh, V.A., Shearer, E.J., Sadeghi, M., Sorooshian, S., Hsu, K., Bolvin, D., Ralph, M.F., 2020. PERSIANN Dynamic Infrared–Rain Rate (PDIR-Now): A Near-Real-Time, Quasi-Global Satellite Precipitation Dataset. Journal of Hydrometeorology 21, 2893–2906. doi: 10.1175/JHM-D-20-0177.1

7. Shearer, E.J., Nguyen, P., Sellars, S.L., Analui, B., Kawzenuk, B., Hsu, K., Sorooshian, S., 2020. Examination of Global Midlatitude Atmospheric River Lifecycles Using an Object-Oriented Methodology. Journal of Geophysical Research: Atmospheres 125, e2020JD033425. doi: 10.1029/2020JD033425

8. O'Brien, T.A., Payne, A.E., Shields, C.A., Rutz, J., Brands, S., Castellano, C., Chen, J., Cleveland, W., DeFlorio, M.J., Goldenson, N., Gorodetskaya, I.V., Díaz, H.I., Kashinath, K., Kawzenuk, B., Kim, S., Krinitskiy, M., Lora, J.M., McClenny, B., Michaelis, A., O'Brien, J.P., Patricola, C.M., Ramos, A.M., Shearer, E.J., Tung, W.-W., Ullrich, P.A., Wehner, M.F., Yang, K., Zhang, R., Zhang, Z., Zhou, Y., 2020. Detection Uncertainty Matters for Understanding Atmospheric Rivers. Bulletin of the American Meteorological Society 101, E790–E796. doi: 10.1175/BAMS-D-19-0348.1

9. Nguyen, P., Shearer, E.J., Ombadi, M., Gorooh, V.A., Hsu, K., Sorooshian, S., Logan, W.S., Ralph, M., 2020. PERSIANN Dynamic Infrared–Rain Rate Model (PDIR) for High-Resolution, Real-Time Satellite Precipitation Estimation. Bulletin of the American Meteorological Society 101, E286–E302. doi: 10.1175/BAMS-D-19-0118.1

10. Sellars, S.L., Graham, J., Mishin, D., Marcus, K., Altintas, I., DeFanti, T., Smarr, L., Crittenden, C., Wuerthwein, F., Tatar, J., Nguyen, P., Shearer, E., Sorooshian, S., Ralph, F.M., 2019. The Evolution of Bits and Bottlenecks in a Scientific Workflow Trying to Keep Up with Technology: Accelerating 4D Image Segmentation Applied to NASA Data, in: 2019 15th International Conference on EScience (EScience). Presented at the 2019 15th International Conference on eScience (eScience), 77–85. doi: 10.1109/eScience.2019.00016

11. Nguyen, P., Shearer, E.J., Tran, H., Ombadi, M., Hayatbini, N., Palacios, T., Huynh, P., Braithwaite, D., Updegraff, G., Hsu, K., Kuligowski, B., Logan, W.S., Sorooshian, S., 2019. The CHRS Data Portal, an easily accessible public repository for PERSIANN global satellite precipitation data. Scientific Data 6, 180296. doi: 10.1038/sdata.2018.296

SELECT CONFERENCE PRESENTATIONS

Oral

1. Shearer, E.J., Yin, G., Li, F., Wood, A., 2022. Advancing Seasonal Prediction of Spring Streamflow in Western U.S. Watersheds: Ensemble Streamflow Prediction (ESP) Weighted by

Climate Oscillations and Sub-seasonal Forecasts of Surface Meteorology. American Meteorological Society Winter Meeting, Virtual

2. Shearer, E.J., Gorooh, V.A., Nguyen, P., Hsu, K.L., Sorooshian, S., 2021. Trend Analysis of Global Tropical Cyclone Precipitation using a High-resolution Climate Data Record. American Geophysical Union Fall Meeting, New Orleans, LA (Press event)

3. Shearer, E.J., Gorooh, V.A., Nguyen, P., Hsu, K.L., Sorooshian, S., 2021. An Object-oriented Analysis into Atlantic Hurricane Precipitation Using a High-Resolution Climate Data Record (invited). American Meteorological Society Winter Meeting, Virtual

4. Shearer, E.J., Nguyen. P., Sellars, S.L., Kawzenuk, B., Analui, B., Hsu, K.L., Sorooshian, S., 2020. Examination of Global Atmospheric River Lifecycle Precipitation Using an Object-oriented Methodology. American Geophysical Union Fall Meeting, Virtual

Poster

5. Shearer, E.J., Nguyen., P., Sellars, S., Sorooshian, S., Hsu, K.L., Kawzenuk, B., Nemani, R., Analui, B., 2019. The Evolution of an Object-oriented Big Data Tool for Analysis of Climate Extremes American Geophysical Union Fall Meeting, San Francisco, CA

6. Shearer, E.J., Nguyen, P., Ombadi, M., Palacios, T., Huynh, P., Furman, D., Tran, H., Braithwaite, D., Hsu, K.L., Sorooshian, S., Logan, W., 2017. Tracking Extreme Rainfall of Hurricanes Harvey, Irma, and Maria through UCI CHRS's iRain System. American Geophysical Union Fall Meeting, New Orleans, LA

Press

7. Intensifying storms and flooding in a changing climate, 2021. American Geophysical Union Fall Meeting, New Orleans, LA

TRAINING

2022	CIRTL@UIC professional development program: Associate level
2021	NCAR/UCAR ASP Colloquia on S2S Forecasts Certificate of Participation
2018–2021	Trainee of the National Science Foundation Ridge to Reef Training Program
2020	AMS Summer Policy Colloquium Certificate of Participation
2019	CW3E Atmospheric River Colloquium Summer School Certificate
2018	Activate to Captivate Engineering Communications Certificate

EXTRACIRRICULARS

2021–2022	Member of AGU Hydrology Section Student Subcommittee (AGU-H3S)
2019–2022	Co-president of UCI's Civil & Env. Engineering Graduate Association (CEEGA)
2018–2019	Board of UCI's Student Chapter of the American Meteorological Society (zotCAMS)

AWARDS

2021	DoD Science, Math, and Research Technology (SMART) Scholarship
2021	CERC-WET Fellow
2021	Outstanding Oral Presentation Award, AMS 34th Conference on Climate Change & Variability
2019, 2020	2x Recipient of NSF's Ridge to Reef Fellowship
2018	Henry Samueli School of Engineering Ph.D. Bridge Fellowship

Abstract of the Dissertation

Unveiling Climate-scale Trends in Hydroclimate Extremes using High-spatiotemporal Resolution Climate Data Records of Precipitation

by

Eric J. Shearer

Doctor of Philosophy in Civil and Environmental Engineering

University of California, Irvine, 2022

Distinguished Professor Soroosh Sorooshian, Co-chair

Assistant Adjunct Professor Phu Dinh Nguyen, Co-chair

Precipitation is a vital component of the water-energy-food nexus and a deadly force of nature responsible for natural hazards like flooding and debris flows. Because of its profound impact to society at large, it is an extremely important variable to measure and predict. Fittingly, the highly variable and chaotic nature of the precipitation field makes quantifying and forecasting arduous. One tool useful for precipitation measurements are satellites, which are capable of measuring precipitation quasi-globally over land and oceans. Given the rapid advancement of remotely sensed observational techniques over the past few decades and the satellite record's recent emergence into climate time scales, new kilometer-scale, sub-daily records of precipitation have been produced capable of high-spatiotemporal insights into some of the most extreme hydroclimate events. With climate change's influence becoming more profound through the passage of time, this dissertation seeks to examine how atmospheric rivers (ARs) and tropical cyclones (TCs) have evolved since the beginning of the satellite age using high resolution climate data records of precipitation (HRPCDRs) and testing for the influence of anthropogenic warming.

In the first half of the dissertation, we adapt the CONNected-objECT (CONNECT) algorithm for the tracking of global mid-latitude AR lifecycles and associated precipitation by implementing a

seeded region growing segmentation algorithm, creating the AR-CONNECT algorithm. One of AR-CONNECT's goals is to track atmospheric water vapor anomalies before evolving into AR geometries, effectively tracking AR genesis farther back than other studies. To accomplish this, AR-CONNECT is without hard-coded geometric criteria yet is still proven to extract synoptic-scale elongated objects >99.99% of the time. With the aid of sub-daily satellite-derived rain data, we investigate the climatology, trends, and patterns of AR lifecycles from 1983-2016 and compare with other AR tracking studies. We find that AR frequency, genesis, and terminus locations are in generally good agreement with other AR tracking methodologies and that AR frequencies in each hemisphere are proportional to the number of AR hotspots. In terms of precipitation, mid-latitude precipitation uncovered by AR-CONNECT shows contributions up to 50% over land and 65% over the ocean. We show that annual values of total rainfall volume, mean size, and mean duration of ARs have increased, conceivably because of greater atmospheric water vapor concentrations from anthropogenic warming. Spatial trend analysis of AR precipitation show increase in precipitation associated with Southern Hemisphere and northern African ARs, among others, but is determined not to be a driver of changes in global precipitation.

In the latter half of the dissertation, we investigate precipitation trends in global TCs. Increases in precipitation rates and volumes from TCs caused by anthropogenic warming are predicted by climate modeling studies and have been identified in several high intensity storms occurring over the last half decade. However, it has been difficult to detect historical trends in TC precipitation at time scales long enough to overcome natural climate variability because of limitations in existing precipitation observations. We introduce an experimental global high-resolution climate data record of precipitation produced using infrared satellite imagery and corrected at the monthly scale by a gauge-derived product that shows generally good performance during two hurricane case studies but estimates higher mean precipitation rates in the tropics than the evaluation datasets. General

increases in mean and extreme rainfall rates during the study period of 1980-2019 are identified, culminating in a 12-18%/40-year increase in global rainfall rates. Overall, all basins have experienced intensification in precipitation rates. Increases in rainfall rates have boosted the mean precipitation volume of global TCs by 7-15%/year, with the starkest rises seen in the North Atlantic, South Indian, and South Pacific basins (maximum 59-64% over 40 years). In terms of inland rainfall totals, year-by-year trends are generally positive due to increasing TC frequency, slower decay over land, and more intense rainfall, with an alarming increase of 81-85% seen from the strongest global TCs. As the global trend in precipitation rates follows expectations from warming sea surface temperatures (11.1%/°C), we hypothesize that the observed trends could be a result of anthropogenic warming creating greater concentrations of water vapor in the atmosphere, though retrospective studies of TC dynamics over the period are needed to confirm.

Chapter 1 - Introduction

1.1. Satellite Remote Sensing of Precipitation

Water resources engineering is a field that is perpetually advancing to meet the water, energy, and food needs of a rapidly changing world. Among the components of the water cycle, precipitation is arguable the most important. Fittingly, it is also very challenging to estimate accurately, especially at high detail and over large domains. This is because two of the most-used tools in measuring precipitation, rain gauges and radar, have significant short-comings in their utility and distribution. Concretely, rain gauges provide localized point measurements that must be extrapolated to provide gridded measurements over larger domains. In the most developed regions of the world, gauge networks are dense enough to represent the "true" rainfall field with a high degree of accuracy. The most notable issues with rain gauges are their limited distributions in remote regions of the world (Sahara Desert, the African and South American rain forest, and the polar regions) and lack of coverage over the oceans and other large bodies of water. Likewise, though ground-based radar can measure the spatial distribution and intensity of rainfall with great accuracy at scales of hundreds of kilometers, blockage by orography makes it a limited tool for use in topographically complex regions like the western U.S. Like rain gauges, ground-based radar stations are limited in their distribution, especially over remote regions of the world, and there are no ground-based radar systems available over the oceans.

Remote sensing of precipitation, done by space-based sensors aboard geostationary and low Earth orbiting (GEO and LEO) satellites, has been shown to be a promising supplement to traditional precipitation measuring techniques and is often the only source of rainfall information for regions of the world without radar and gauge coverage. Satellite remote sensing in general (depending on the product) feeds measurements of visible and infrared light from GEO satellites and naturally emitted

microwave energy from LEO satellites to empirical or black-box precipitation-estimating models. Satellite remote sensing is a newly developing field seeing rapidly improvements thanks to advances in data-driven tools from the field of computer science, like machine learning and deep learning, which help detangle highly chaotic systems like the hydroclimate (Akbari Asanjan et al. 2018; Pan et al. 2019; Hayatbini et al. 2019; Gorooh et al. 2020). Such advances have made satellite remote sensing a vital tool for a wide array of applications across the field of water resources engineering.

Satellite remote sensing products come in many shapes and flavors: some products aim to use all tools available to provide the best measurement of precipitation at a given snippet of time. These include Precipitation Estimates from Remotely Sensing Information using Artificial Neural Networks (PERSIANN; Hsu et al. 1997; Sorooshian et al. 2000), Integrated Multi-satellitE Retrievals for GPM (IMERG), among others. Other products forego the low-resolution passive microwave (PMW) measurements in order to preserve high resolution and short latency periods, for example the PERSIANN-Cloud Classification System (PERSIANN-CCS; Hong et al. 2004) and the PERSIANN Dynamic Infrared Rain rate-Now (PDIR-Now; Nguyen et al. 2020a,b) products provide measurements of precipitation at 0.04° and hourly spatiotemporal resolution with a latency period of 15 minutes to an hour. These products are good for near real-time estimates of precipitation that are required for rapid hazard response and flood forecasting. Lastly, products with a sufficient period of data (generally, at least 30 years) can use well-maintained gauge records or gauge-derived products to correct temporal and spatial inhomogeneity and produce climate data records (CDRs) of precipitation useful for long-term trend analysis.

1.2. Climate Change Impacts on Precipitation

Within the scientific community and beyond, there is little scientifically rigorous dispute to the assertion that anthropogenic increases in atmospheric concentrations of greenhouse gases have

created detectable shifts in the climatology of global air and sea temperature. These changes in turn affect related Earth system variables: an increase in air and ocean temperatures causes melting glaciers which raise sea level height while ocean acidification is occurring because of greater carbon dioxide (CO_2) storage by the ocean, supplied by the atmosphere.

It is expected that anthropogenic warming should create changes in the intensity and dynamics of the global rain fall field (Nguyen et al. 2018b). For instance, greater sea surface temperature (SST) values increase atmospheric evaporation rates. When coupled with increases in the water-holding capacity of air from increased temperatures—governed by the Clausius–Clapeyron relation at a rate of ~7%/°C—produces greater potential for wetter and more frequent extreme events as regions shift from a water-limited to energy-limited precipitation regime. Likewise, changes in atmospheric circulations caused by anthropogenic climate change—for instance, storm tracks (Trenberth 2011)—can shift the distribution of rainfall climatology and cause desertification and similar regional climate classification changes.

Presently, there are two prominent hypotheses for how global rainfall may change in an anthropogenically warmed climate: 1) region-specific intensification (i.e. dry getting drier and wet getting wetter), and 2) increases in global hydroclimate extremes. There exists little evidence for the former conclusion; in Greve et al. (2014), the authors find that only 10% of global land coverage by area has seen changes fitting the "dry getting drier, wet getting wetter" pattern. However, there is considerable evidence that climate change has influenced the record-breaking rainfall totals of some of the most prolific extreme events since the new millennium, namely Hurricanes Katrina, Harvey, Irma, Maria, and Florence, among others. Still, global attempts at retrospective trend analysis of hydroclimate extremes at the climate scale have been difficult owing to shortcomings in the historical observation period, beginning at the turn of the satellite age in the last 1970s. As mentioned in Section

1.1, ongoing research has increased the utility of these measurements. This, combined with the passage of time, has begun to allow for the first multi-decadal analyses of hydroclimate extremes and their precipitation.

1.3. Research Motivation

As anthropogenically driven warming of the climate increases atmospheric moisture concentrations, there is evidence that similar increases in extreme precipitation of hydroclimate extremes like atmospheric rivers (ARs) and tropical cyclones (TCs) will be observed (Wuebbles et al. 2017; Espinoza et al. 2018; Walsh et al. 2019). With the aid of multi-decadal, high-resolution, and high-quality CDRs of precipitation, we retrospectively observe precipitation trends in the lifecycles of hydroclimate extremes. Concretely, for this dissertation, we overview two scientific reports published in academic journals that overview the development of catalogs of 1) global mid-latitude ARs from 1983-2016 using NASA Modern-Era Retrospective analysis for Research and Applications v.2 (MERRA-2) integrated water vapor transport (IVT) data with PERSIANN-CDR precipitation data and 2) global TCs from 1980-2019 using experimental high-resolution PDIR-Now bias corrected by Global Precipitation Climatology Project (GPCP) v2.3 monthly gauge data are showcased. The climate-scale trends of storm lifecycle characteristics data-mined from these catalogs are examined using the object-oriented analysis technique to determine if and how these hydroclimate extremes are intensifying over time scales of sufficient length to suggest a changing climate.

As the field of AR tracking is relatively new, the development of our AR tracking methodology includes analysis into trends in the size, frequency, and lifecycle duration, along with a comparison of AR-CONNECT to other AR tracking methodologies. Essentially, precipitation is not the sole focus of the former study. The latter, however, is exclusively focused on TC precipitation trends.

A concise introduction in Chapter 2 provides an overview of hydroclimate extremes and the satellite precipitation products and statistical tools utilized to conduct the scientific inquiries included in this dissertation. The projects themselves are introduced in Chapters 3 and 4, based on the articles 1) "Examination of Global Midlatitude Atmospheric River Lifecycles Using an Object-Oriented Methodology" (Shearer et al. 2020) published in the Journal of Geophysical Research – Atmospheres from the American Geophysical Union publishing company and 2) "Unveiling Four Decades of Intensifying Precipitation from Tropical Cyclones Using Satellite Measurements" (Shearer et al. 2022) in production in Scientific Reports from the Springer Nature publishing company. Lastly, dissertation-wide conclusions are provided in Chapter 5, along with musing on feasible future directions for related studies given the current state of the field.

Chapter 2 – Background

2.1. High-resolution Climate Data Records of Precipitation

During the last decade, consistent remote sensing measurements useful for precipitation estimation crossed a major milestone and became useful for climate-scale studies (according to the 30-year standard observed by many climatologists). With cutting-edge research rapidly improving the skill of satellite quantitative precipitation estimation (QPE), satellite QPE techniques increasingly entered the realm of practical applications (especially non-real time measurements that can be bias corrected by additional satellite, radar, and *in situ* measurements). The production of high-quality, quasi-global CDRs of precipitation measurements with high spatiotemporal resolution soon followed. Based on the architecture of the PERSIANN algorithm while incorporating high-quality gridded monthly gauge data, the PERSIANN-CDR data set was produced (Ashouri et al. 2015), spanning from 1983 to the present day at a temporal resolution of daily and a spatial resolution of 0.25°x0.25° (approximately 25

km) from 60°S-60°N. Years later, in the pursuit of producing high-resolution precipitation CDRs (HRPCDRs), the high-resolution PERSIANN-CCS and PDIR-Now models were fed IR data back to the beginning of the satellite age and bias corrected by monthly gauge data, making them available from the early 1980s to the current day at a gridded resolution of 0.04°x0.04° and sub-daily temporal resolution, producing the PERSIANN-CCS-CDR and PDIR-CDR data sets. HRPCDRs, although considerably less accurate than PERSIANN-CDR owing to their greater spatiotemporal resolution, and therefore their higher propensity to being plagued by measurement noise, are still shown to be superior in calculating extreme precipitation (Sadeghi et al. 2021b), making them especially useful for small and extreme storms like mesoscale convective systems and TCs.

2.2. Big Data

In this modern age, scientists have access to unprecedented volumes of Earth science data thanks to the rise and commercialization of the satellite age; exponential increases in computing power driving constant development of new-and-improved micro- to global-scale models of weather, climate, oceans, land surface, etc.; increased gridding of vital *in situ* measurement networks; among other sources. Thanks to cloud storage and cloud computing, there has never been more opportunities for investigators to access the wealth of data that currently exists. The sheer volume of data and its projected rapid growth have brought Earth science research into the age of "Big Data" (Hey et al. 2009). Advancements in the age of big data are characterized by problem solving not through revolutionary methods or extraordinary insight, but through uncovering hidden patterns using data mining techniques in massive volumes of data. For example, researchers at CERN analyzed data recorded from 800 trillion particle collisions to uncover the existence of the Higgs Boson. More relevantly, big data in hydrology is being explored to improve hydrologic modeling of streamflow, evapotranspiration, etc. (Chen and Wang 2018).

Due to the high level of detail and long temporal extents of HRPCDRs like PERSIANN-CCS-CDR and PDIR-CDR, their data records encompass terabytes of memory and can make processing a challenging endeavor. We classify these projects as big data and must employee tools from the field of data science to data mine relevant information, like machine learning, deep learning, and object-oriented analysis.

2.3. Object-oriented Analysis

Though a prominent tool used in many modern Earth science studies, machine learning is far from the only effective tool in the age of big data. Introduced in Sellars et al. (2013), the authors utilize a technique known as object-oriented analysis. Object-oriented analysis is a technique where populations of "objects", which are identified items, events, etc. that can be identified and segmented from large volumes of data are described and statistically analyzed by their attributes (Figure 3.1). For example, a collection of hydroclimate extremes can be analyzed by the distribution of their sizes, locations, durations, etc. Object-oriented analysis has noteworthy benefits for hydroclimate studies: events are discretely counted and recorded, meaning they can be examined individually, or their population considered statistically, from techniques as simple as calculating averages and percentiles to distribution tests and cluster analysis.

2.4. The CONNected-objECT (CONNECT) Algorithm

The CONNected-objECT (CONNECT) algorithm is a big data algorithm that uses connectivity (overlap) to segment, group, and track elevated or anomalous data signatures in large volumes of data using a flood-filling algorithm (Pavlidis 1979; Figure 3.1). It was developed to study hydroclimate extremes, but the simplicity of its design means its utility exists across disciplines in the Earth sciences.

CONNECT uses three-dimensional (x,y,t) voxels of a target variable (e.g. rainfall) to construct objects where voxels with intensities above a user-defined threshold are contiguous over space and time. As grouping voxels across the time axis captures the evolution of an object from genesis to terminus, CONNECT performs well as a tracking algorithm, meaning objects segmented by CONNECT are the lifecycles of weather phenomena. CONNECT auto-calculates object characteristics, such as spatiotemporal properties like volume, speed, duration, etc. and outputs it into a table for statistical/object-oriented analysis.

The CONNECT methodology was first developed for segmenting extreme rainfall events using the PERSIANN rainfall dataset (Sellars et al. 2013, 2015; Sadeghi et al. 2021a). Subsequent work with CONNECT used the IVT variable to track atmospheric rivers (ARs): long, transient corridors of enhanced water vapor fluxes that frequently produce heavy orographic precipitation in the mid-latitudes (Dettinger 2011). However, using IVT to track ARs with CONNECT was limited by difficulties. First, as IVT values at lower levels (<500 kg/m/s) exist in the atmosphere for prolonged periods in the tropics, which results in multiple events of enhanced IVT being combined into a single "conglomerate" object—not ideal for the extraction of singular AR lifecycles—the study had to be done with a more extreme IVT threshold of 750 kg/m/s. Moreover, IVT-CONNECT extracts a multitude of tropical and non-AR activity. Due to these shortcomings, the study in (Sellars et al. 2017) was simplified to only look at extreme IVT objects and was explicitly stated to not be an AR-specific methodology. However, the need to adapt CONNECT for ARs still existed, especially as the field of AR tracking emerged.

2.5. Atmospheric Rivers

The distribution and transport of atmospheric water vapor is a critical component of California's water cycle. ARs are one of the most important hydrometeorological phenomenon and a prime source of

water in the region. ARs are the transient and narrow atmospheric pathways that transport water that has evaporated from the ocean (Ralph and Dettinger 2011) with flux magnitudes that can be greater than the output of the Amazon River. ARs frequently produce heavy precipitation over the U.S. west coast, especially where they are forced upward by orography (e.g., Sierra Nevada Mountains in California; Ralph et al. 2004). Partially owing to its complex topography, scientists estimate that AR events contribute to ~30-50% of coastal Southern California's precipitation (Dettinger 2013), and are agents of extraordinarily favorable and extremely unfavorable phenomena in the region. On the one hand, ARs have been found to replenish reservoirs and end droughts (Dettinger 2011, 2013; Guan et al. 2010) such as the recent (2013-2016) California drought (with 50% of the state in exceptional drought status) that caused substantial stress to the vital irrigation and water supply infrastructure of the state. On the other hand, high amplitude AR events can also cause devastating floods and debris flows (Neiman et al. 2013; Ralph and Dettinger 2011; Dettinger 2011; among others), similar to the deadly mudslides in Montecito in January, 2018, that resulted in 21 fatalities and hundreds of millions in damages. Concretely, Ralph et al. (2006) found that in the Russian River basin in Northern California, all seven recorded major flooding events that occurred were associated with AR events.

While ARs and their impacts, which range from very beneficial to very detrimental, have traditionally been studied as a western U.S. phenomenon (Rutz et al. 2014), it has become apparent that ARs affect many low-, middle-, and high-latitude regions of the world with similar affects to those observed in California (Dezfuli 2020; Wille et al. 2019; Gorodetskaya et al. 2014; Ramos et al. 2015; Thapa et al. 2018; Viale et al. 2018; Zhou et al. 2018; Esfandiari and Lashkari 2021; to name a few).

2.6. Tropical Cyclones

TCs are among the most devastating and deadly climate phenomena observable globally (Rappaport 2014; Bakkensen and Mendelsohn 2019). Extreme precipitation produced by TCs, especially when

coupled with wind-enhanced storm surge, culminate to produce some of the most significant flooding damages every year (Dube et al. 2009; WorldBank 2010; IPCC 2012; Mendelsohn et al. 2012; Weinkle et al. 2012). For example, Hurricane Harvey dropped an unprecedented 1.5 meters of rainfall over the greater Houston metropolitan region (van Oldenborgh et al. 2017; Domingues et al. 2021) while Typhoon Haiyan caused a catastrophic emergency in the Philippines due to the combination of high storm surge and extreme rainfall totals (Nguyen et al. 2014).

Future climate projections ubiquitously predict increased TC precipitation into the year 2100 (Wuebbles et al. 2014, 2017; Seneviratne et al. 2012; Musser et al. 2017; Easterling et al. 2017; Lin et al. 2015; Villarini et al. 2014; Patricola and Wehner 2018; Knutson et al. 2020; IPCC 2021). The intensification of precipitation by anthropogenic warming has been observed in some of the most intense and recent TCs in the North Atlantic basin, namely Hurricane Katrina, Irma, Maria (Patricola and Wehner 2018), Harvey (Risser and Wehner 2017; van Oldenborgh et al. 2017), and Florence (Reed et al. 2020). Regional increases in TC activity have been detected in North America (Maxwell et al. 2021; Paerl et al. 2019; Touma et al. 2019), South and Southeast Asia (Gao et al. 2021; Liu and Wang 2020; Chang et al. 2013), and Australia (Balaji et al. 2018). However, (1) despite the apparent intensification of TCs in the last few years, (2) the consistent projection of increased TC precipitation by global and regional climate models, and (3) the proven anthropogenic influence on TC precipitation in select regions and case studies, the hypothesis that there has been a historical change in global TC precipitation activity has not reached a consensus in the global community owing to the large natural variability characteristic of TC events (Kossin 2018; Landsea et al. 2010; Knutson et al. 2010; Peterson et al. 2013) and imitated observations in the early satellite age.

Chapter 3 – Detection and Trend Analysis of Atmospheric River Lifecycles

3.1. Introduction

A recent report by the U.S. Global Change Research Program highlights that the frequency and severity of landfalling ARs will likely increase as a result of increased evaporation and higher atmospheric water vapor content caused by increasing global temperatures (Wuebbles et al. 2017). As previously discussed, the negative impacts of ARs are frequently quite extreme. Hence, it would be beneficial to decision makers to have as much forewarning as possible to prepare for mitigation efforts against the extreme winds and rainfall during strong AR activity. Improving our confidence in understanding AR environments and how they are likely to change going into the future is of vital importance. Thus, advancing the tools to observe and study these events is vital for mitigating losses and maintaining water security.

As ARs have emerged in the scientific consciousness as a global phenomenon, the need to classify ARs globally has birthed a multitude of definitions and methodologies that attempt to unify the definition of ARs (Shields et al. 2018; Rutz et al. 2019; O'Brien et al. 2022; Collow et al. 2022). From an impacts point of view, the differing geography and climate patterns across AR-affected regions make direct comparisons of AR intensity-impact relationships variable, creating difficulty in determining a one-size-fits-all threshold of IVT for global AR segmentation. Difficult as it may be, numerous studies have attempted to unify a definition of ARs using an absolute IVT definition (Rhoades et al. 2020; Rutz et al. 2014; Sellars et al. 2017) or relative definition, such as latitude-dependent (Lavers and Villarini 2015) or pixel-based (Brands et al. 2017; Guan and Waliser 2015).

ARs exist on synoptic time scales and travel distances of thousands of kilometers, requiring the development of tracking algorithms to study ARs from genesis to terminus (lifecycles.) One such methodology is the CONNECT algorithm, which extracts hydroclimate features where they are contiguous over space and time. While not AR-specific, CONNECT run on IVT was invaluable for studies by the Atmospheric River Tracking Method Intercomparison Project (ARTMIP; Shields et al. 2018; Rutz et al. 2019; O'Brien et al. 2022; Collow et al. 2022). Other AR lifecycle methodologies include (Payne and Magnusdottir (2014), Zhou et al. (2018), and Guan and Waliser (2019), all of which are either based on a relative IVT threshold and/or are North American-centric.

In this study, the framework of CONNECT is altered to better extract ARs (hereafter, AR-CONNECT). A seeded region growing segmentation methodology with static IVT thresholds is introduced to segment single AR lifecycles, offering an alternative to the methodologies introduced in Zhou et al. (2018) and Guan and Waliser (2019) to handle combination and separation in AR tracking. In this paper, we introduce the AR-CONNECT methodology and investigate the climatology, trends, and patterns of global midlatitude AR lifecycles and associated rainfall.

3.2. Data

3.2.1. MERRA-2 Integrated Water Vapor Transport

IVT is a vector that describes the movement of atmospheric water vapor. The IVT measurements used to produce this data set were derived from the NASA Modern-Era Retrospective Analysis for Research and Applications-version 2 (MERRA-2) data (Gelaro et al. 2017), calculated from the following formula and used in the Tier 1 ARTMIP analysis—data ranges from January 1980–June 2017:

$$\overrightarrow{IVT} = -\frac{1}{g}\int_{p_{sfc}}^{p_{200}} q\vec{V}\, dp$$

where p is pressure (hPa), p_{200} is the pressure at the 200 hPa level, p_{sfc} is pressure at the Earth's surface, q is specific humidity at height p, $\vec{V}$ is wind velocity (m/s), and g is gravitational acceleration. MERRA-2's high spatiotemporal resolution, proven accuracy, and emphasis on the hydrologic cycle (Rienecker et al. 2011) make it an invaluable tool for AR research. Moreover, MERRA-2's utility in producing the analysis done in Sellars et al. (2017) and proven skill for AR detection (Jackson et al. 2016; Martin Ralph et al. 2019; Guan and Waliser 2019) further cement its benefits for AR research.

3.2.2. PERSIANN-CDR Precipitation

PERSIANN-CDR is a multi-decade climate data record (1983 to present) of global precipitation that spans 60°N to 60°S with a spatiotemporal resolution of 0.25° and daily, derived from the PERSIANN algorithm and bias-adjusted using the GPCP monthly product. The quality of PERSIANN-CDR has been continuously evaluated by external researchers and compares very favorably to the ground truth and other global satellite products (Guo et al. 2016; Miao et al. 2015; Ombadi et al. 2018). PERSIANN-CDR's performance and quasi-global extent give the researchers in this study an opportunity to probe into the patterns and trends of global AR precipitation. PERSIANN-CDR is available from the CHRS Data Portal (Nguyen et al. 2019).

Given that MERRA-2 has a temporal resolution of three-hourly, we opted to use three-hourly PERSIANN-CDR data for rainfall mapping. Three-hourly PERSIANN-CDR (PERSIANN-CDR) should be considered experimental, as it's primarily used to produce publicly available PERSIANN-CDR data through daily averaging. As the time resolution is higher, there are issues with missing coverage. Therefore, for the rain trends plotted for section 4.3, only areas where there is coverage for at least 90% of the time steps are considered. Given three-hourly PERSIANN-CDR's sub-daily resolution, it can be considered an HRPCDR like PERSIANN-CCS-CDR and PDIR-CDR, though its spatial resolution is much coarser.

Analysis in this chapter is done during the period where the MERRA-2 and PERSIANN-CDR data overlap to the last year of complete coverage: 1983–2016. Both variables are measured over simultaneous time windows, from 00z to 03z, 03z to 06z, etc. It should be noted that PERSIANN-CDR is an accumulative quantity, while IVT from MERRA-2 is a temporal average.

3.3. Methods

For this study, the CONNECT methodology was adapted to study the lifecycles of ARs at three-hourly time steps (data resolution of the IVT variable from MERRA-2). The following criteria were introduced to and adapted from CONNECT to create the AR-CONNECT framework:

- To overcome the challenges of conglomerate objects and henceforth isolate singular AR events, a seeded region growing segmentation technique (Adams and Bischof 1994)was introduced.
- To filter out tropical moisture features such as tropical cyclones and monsoons, objects with centroids inside of the tropical latitudes of 23.25°N–23.25°S are filtered out. This means that an AR's genesis can be tropical, but the bulk of its volume should be primarily in the mid-to-upper latitudes.
- Sellars et al. (2017)'s minimum duration criteria of 24 hours is included in the AR-CONNECT methodology.
- To quantify rainfall totals, experimental three-hourly PERSIANN-CDR data are mapped to AR-CONNECT objects.

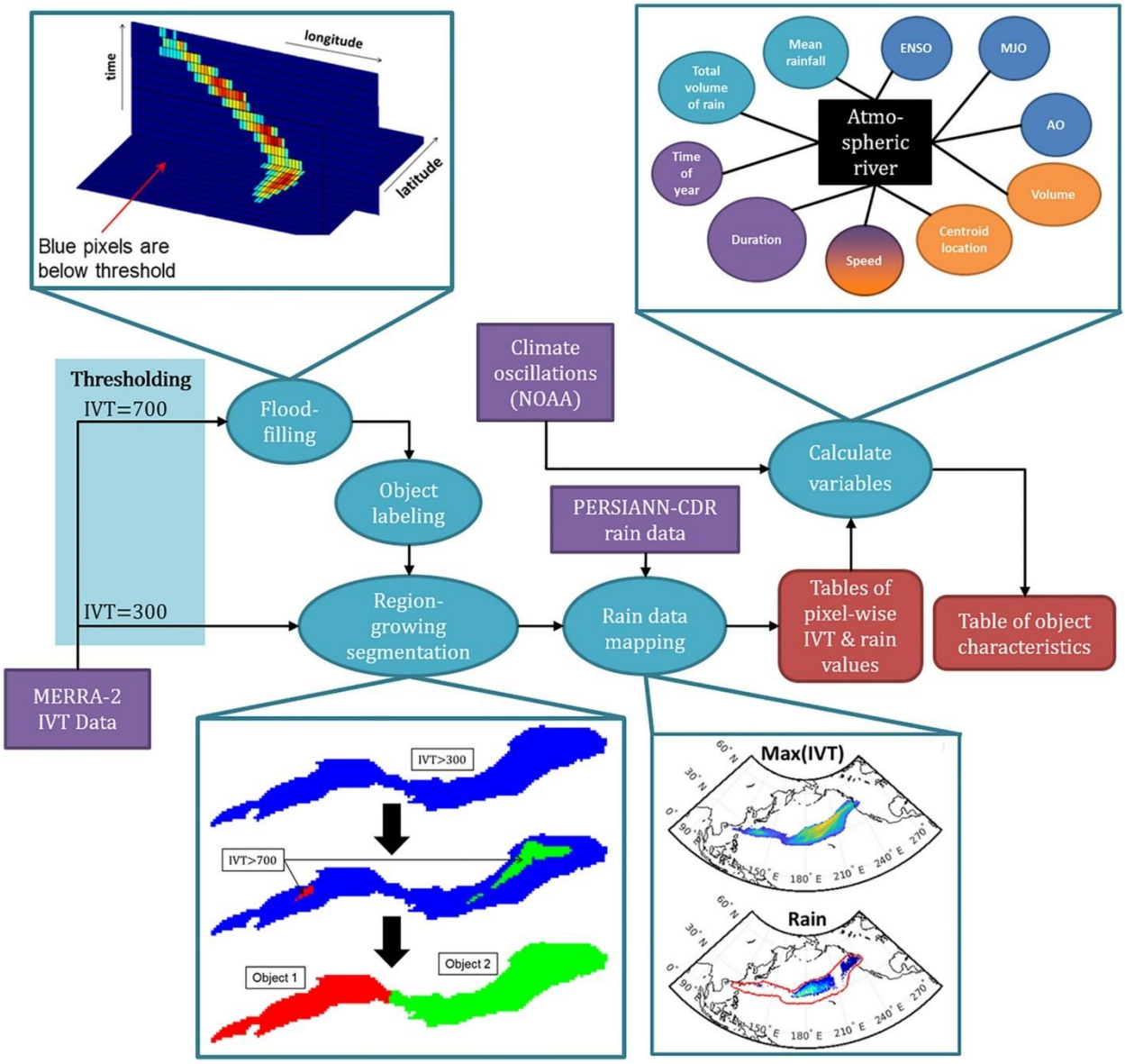

Figure 3-1. Schematic of the AR-CONNECT algorithm's atmospheric river (AR) tracking method, with graphics for important processing steps. Purple indicates data inputs, blue demarcates processing steps, and red represents the output products of AR-CONNECT. Processing steps can be summarized thusly: integrated water vapor transport (IVT) data is thresholded at two levels, IVT=300 (AR body) or the IVT=700 (AR core). Flood-filling involves finding all regions where IVT values at core levels are contiguous over time and space. This is the tracking portion of the AR-CONNECT methodology. Object-labeling involves giving each AR core object a unique identification number. Region-growing segmentation is the process of growing the cores of an AR body, separating the AR body into individual AR lifecycles (labeled by the cores' object labels) at the IVT=300 level. Rain data mapping is the process of mapping 3-hourly PERSIANN-CDR to AR-CONNECT objects. Lastly, AR-CONNECT auto-calculates lifecycle characteristics like duration, speed, extent, rainfall volume, and many more.

3.3.1. Region Growing Segmentation and Thresholding

Region growing segmentation assumes that ARs have a core of enhanced IVT magnitude and uses this core to track and segment regions of enhanced IVT, similar to the methodology of (Mundhenk et al. 2016). However, AR-CONNECT differentiates itself from other methodologies because it tracks where cores are contiguous over time and space before thresholding, meaning AR cores and bodies can be disconnected during one timestep prior to later combination. At the same time, a region of enhanced IVT can be divided into several AR bodies equal to the number of cores within the boundary.

The thresholds utilized for the region growing technique are 700 and 300 kg m^{-1} s^{-1} for the AR core (seed) and the AR boundary (body), respectively. The threshold of 700 kg m^{-1} s^{-1} was adapted from the IVT-CONNECT700 catalog in Shields et al., (2018), which was found to capture the high-intensity cores of strong ARs and suffers very little from the conglomerate object problem thanks to its increased threshold. The 300 kg m^{-1} s^{-1} threshold for the AR boundary is a rough average of the thresholds from Rutz et al. (2014; 250 kg m^{-1} s^{-1}), Ramos et al. (2018; 346–373 kg m^{-1} s^{-1}), and the range of thresholds calculated in Guan and Waliser (2015; 100–500 kg m^{-1} s^{-1}). The slightly elevated threshold of 300 kg m^{-1} s^{-1} means AR-CONNECT's utility is best in the mid-latitudes, rather than at the poles.

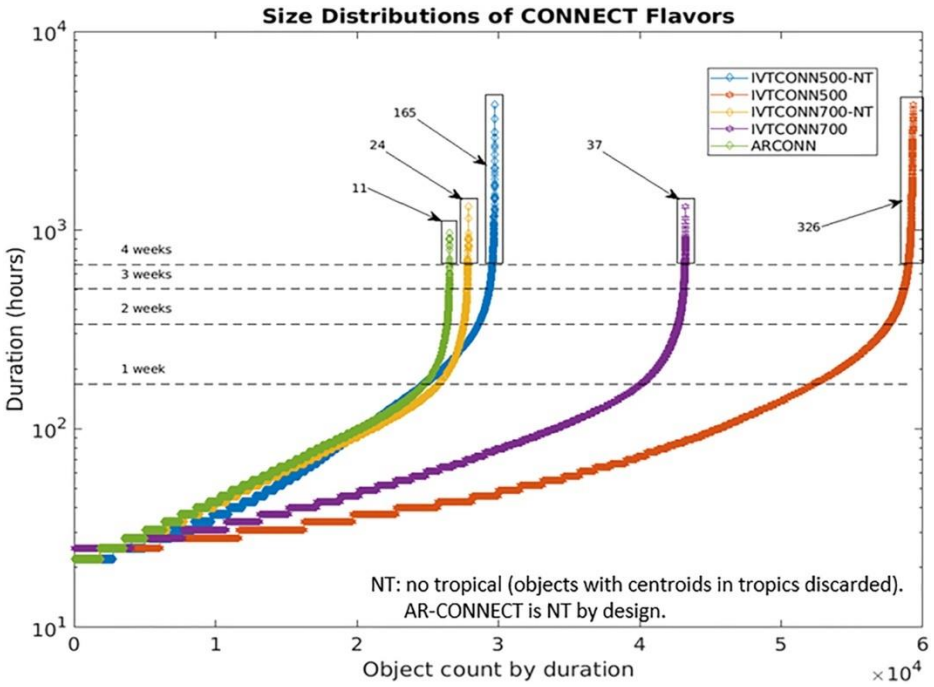

Figure 3-2. Atmospheric river (AR) lifecycle durations depending on methodology. In the legend, the number indicates the integrated water vapor transport (IVT) threshold used (300 kg m^{-1} s^{-1} for AR-CONNECT), and "NT" indicates the filtering of the parent algorithm's tropical objects (included in the AR-CONNECT framework). Numbers with arrows indicate the count of objects greater than 4 weeks in duration. Atmospheric dynamics implies that objects greater than a few weeks shouldn't be considered singular AR events and are considered conglomerate objects. This is reflected by the choice to use 2 weeks as the maximum duration for AR objects.

3.3.2. AR-CONNECT as an Atmospheric River Detection Technique

AR-CONNECT is developed to be a permissive algorithm, *i.e.,* a methodology that more frequently categorizes IVT fluxes as an AR, as its design was implemented, in part, to study global rainfall—a more restrictive design would cause significant underestimates to global rainfall totals. Moreover, AR-CONNECT aims to determine the genesis of ARs before growing to the geometric size or shape criteria commonly used in AR studies, *i.e.*, length >2,000 km, width <1,000 km (Wick et al., 2013). Because AR-CONNECT has no requirements for length, width, or shape, one may suspect that AR-CONNECT is a misnomer—not properly designed to track ARs, which are officially defined as "long, narrow" (Ralph et al. 2018), but rather a methodology to study regions of enhanced IVT. However, analysis shows that 99.99% are >2,000 km in length for at least one timestep in its lifecycle and 89%

of the AR-CONNECT objects have a length-to-width ratio of >2 and 97% have a ratio of >1.5. Lastly, we consider the shape index (AghaKouchak et al. 2011), a metric used to calculate the geometry of objects, at the object's greatest length. To be considered appropriately elongated, we set a minimum threshold of <0.75 based on Figure 7b from AghaKouchak et al., (2011), which shows an elongated object reminiscent of AR geometry. At this threshold, >99.99% of objects have a lower shape index. Furthermore, 97% of objects are lower than a more extreme shape index threshold of 0.60 and 88% are <0.50. With all these metrics considered as a whole, we conclude that objects segmented by AR-CONNECT show strong evidence of being both long and thin, circumventing the need to hard-code strict geometric criteria.

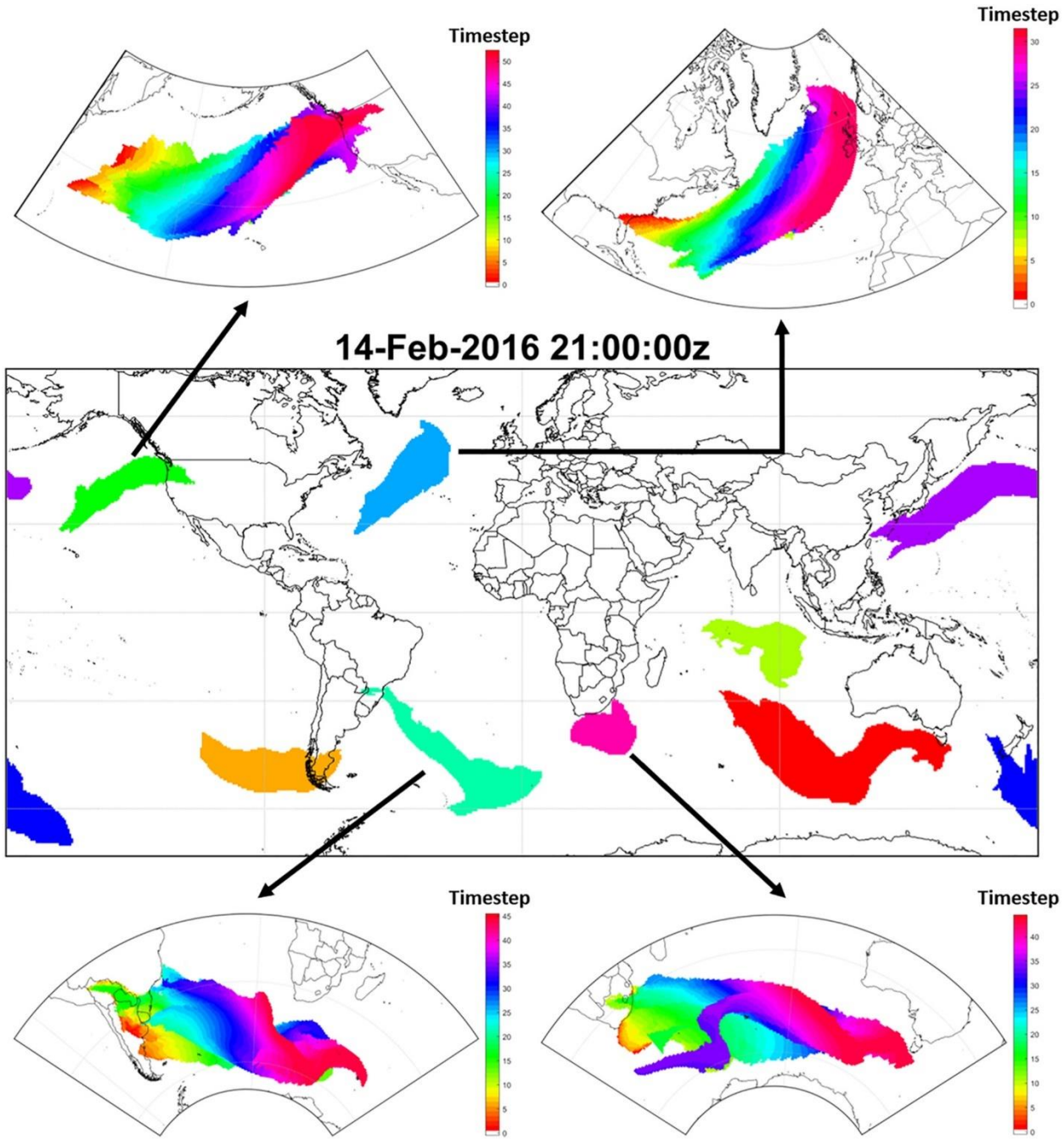

Figure 3-3. AR-CONNECT objects on 14 February 2016 at 21:00z. The lifecycles of four atmospheric rivers (ARs), with pathways over the northern Pacific Ocean, the northern Atlantic Ocean, the southern Atlantic Ocean, and the Indian Ocean, are plotted to showcase their evolution and movement over their lifecycles. Of particular note is the AR over South Africa, which begins as a circular blob of IVT rather than an elongated shape more associated with ARs, subsequently evolves into longer and more elongated shapes over its lifecycle. This demonstrates one of the goals of AR-CONNECT: to identify ARs' origins before they resemble AR shapes.

3.3.3. Comparison to other Atmospheric River Tracking Methods

To showcase AR-CONNET's utility in the emerging field of AR tracking, we compare it to three pioneering methodologies: Payne and Magnusdottir (2014), Zhou et al., (2018), and Guan and Waliser (2019). The tracking methodology of Payne and Magnusdottir (2014) was developed to track large-scale ARs that made landfall on the West Coast of North America. The requirements for the algorithm, a discrete minimum areal size of 21,000 km^2 and a static IVT threshold of 350 kg m^{-1} s^{-1} are too restrictive to capture the geneses of lifecycle ARs, making AR-CONNECT's ability to capture locations of AR genesis and its quasi-global extent a notable improvement over this methodology. Zhou et al. (2018) uses a relative IVT threshold based on the 85^{th} percentile of IVT per geographic location and season. Like Payne and Magnusdottir, Zhou's methodology is North American-centric. The AR tracking algorithm from Guan and Waliser (2019), named tARget (v.3), utilizes a relative threshold $>85^{th}$ percentile like Zhou et al. (2018). Climatological-based methodologies continually demonstrate great utility, but their thresholds are not linked to impacts. Therefore, AR-CONNECT's usefulness exists in its threshold at levels where AR impacts are observable.

The biggest difference between AR-CONNECT, tARget, Zhou's methodology, and the IVT-CONNECT methodology from Sellars et al. (2017) is its treatment of separation, combination, and deformation, the background of which is explained in depth in Guan and Waliser (2019). Succinctly, IVT-CONNECT treats the combination of all IVT objects as a singular object, not treating the combination, division, or deformation of an AR as an AR genesis or terminus. Zhou and tARget both consider combination, division, and deformation in determining the genesis/terminus of ARs, but while Zhou considers each division or combination the start of a new AR, tARget aims to distinguish which AR is most similar from the previous step and assigns it to the next. For example, during a combination (2 ARs combining into 1; 2→1), tARget determines which AR from the previous step is most like the newly combined AR, and assigns them the same identification number, while the other

AR is considered terminating. Alternatively, during a separation (1 ARs dividing into 2; 1→2), whichever AR is most like the AR from the previous step is considered a continuation, while the other is considered a genesis. AR-CONNECT, like IVT-CONNECT, elects to not consider combination, division, or deformation in AR tracking, preferring to segment based on AR cores. The advantage of this can be seen in Figure 3.4, where an idealized scenario of two ARs with distinct cores going through separation then combination is only successfully labeled according to their cores by the AR-CONNECT methodology.

3.4. Results

The AR-CONNECT catalog currently consists of AR lifecycle objects described by a multitude of characteristics including hydroclimate variables such as the average, maximum, median, sum, and standard deviation of the IVT field and the precipitation field; spatiotemporal variables such as each object's average areal extent, speed, duration (number of timesteps from genesis to terminus multiplied by its three-hour temporal resolution), lifecycle centroid (weighted centroid of IVT over the event's lifecycle), genesis and terminus location, and genesis to terminus extent; and the states of 40 climate oscillation time series, including the Arctic Oscillation (AO), El Niño Southern Oscillation (ENSO) time series such as the Multivariate ENSO Index (MEI), North American Oscillation (NAO), and many more.

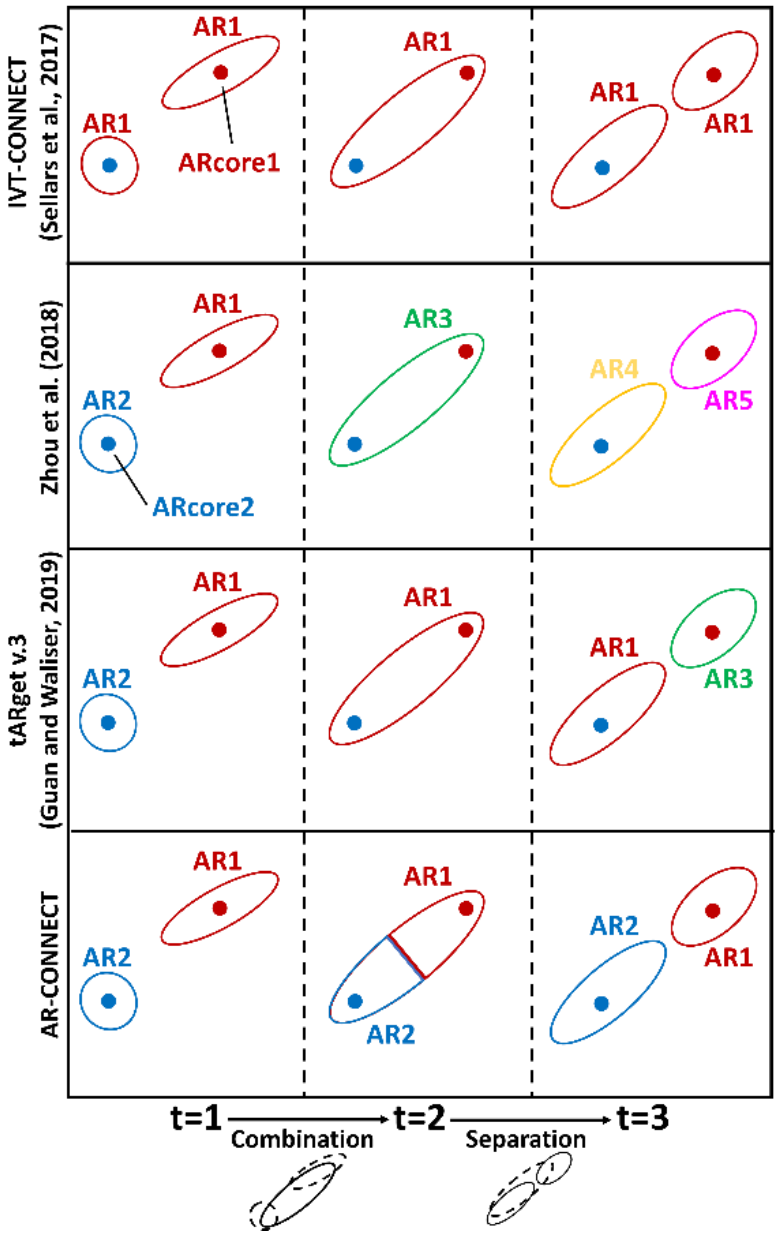

Figure 3-4. A comparison of how four different atmospheric river (AR) tracking methodologies handle a scenario where two AR bodies go through combination then separation over three time steps (t). The colored shape outlines, labeled as AR1–5 and color-coded, represents the body of the AR over each step of its lifecycle, while the filled color-coded dots, identified as ARcore1–2, represent the core of the AR (in this scenario, these cores are spatiotemporally contiguous per the requirements of AR-CONNECT.) Of each methodology, AR-CONNECT segments the lifecycle of ARs equal to the number of AR cores, while IVT-CONNECT combines all AR bodies into one lifecycle, Zhou et al. (2018) produce new ARs at every time step for a total of five, and tARget v.3, while showing skill in tracking ARs across the complicated scenarios inherent to AR tracking, does not track consistently with the AR core identities, falsely identifying the region surround ARcore2 as AR1.

3.4.1. Climatology

Table 3-1. The mean, minimum, maximum, and standard deviation of the annual frequency of atmospheric rivers (ARs) per year and the annual averages of three important characteristics of AR lifecycles: average discrete area, duration, and distance from the equator. Values belonging to global ARs are in black, while values of ARs that inhabit the Northern and Southern Hemisphere are identified in red and blue, respectively.

	Mean	Minimum	Maximum	Std. Dev.
Frequency of ARs	764	724	812	19.4
	312	286	339	10.6
	452	407	494	16.9
Average discrete area (km^2)	3.09×10^6	2.98×10^6	3.24×10^6	6.34×10^4
	2.92×10^6	2.77×10^6	3.18×10^6	8.59×10^4
	3.21×10^6	3.04×10^6	3.42×10^6	8.22×10^4
Duration (days)	3.12	2.99	3.28	7.07×10^{-2}
	3.25	3.07	3.41	8.96×10^{-2}
	3.04	2.88	3.22	8.75×10^{-2}
Distance from the equator (°)	39.8	39.0	40.6	0.389
	39.4	38.3	40.3	0.557
	40.0	39.4	41.0	0.471

When considering global ARs, we see an average of 764 ARs per year, each with an average discrete size of 3.09 million km^2, lasting for an average of 3.12 days with a center of mass at 39.8 degrees from the equator. When looking at hemispheres, we see that there are a smaller number of Northern Hemisphere ARs, which are smaller in volume but greater in duration and closer to the equator than southern hemisphere ARs. The ratio of AR counts per year between the Northern and Southern Hemisphere follow a ratio of approximately 2:3, which is equivalent to the number of AR hotspots observed in Figure 3.5a and found in Sellars et al. (2017) and Guan and Waliser (2019). Furthermore, we see that AR activity is minutely more stable in the Northern Hemisphere than in the Southern Hemisphere, where the standard deviation of annual AR counts is only 3.2% of the annual mean, compared to 3.7%. This is the only variable where the standard deviation is smaller in the Northern Hemisphere than the Southern Hemisphere, which in general have more consistency in the spatiotemporal characteristics studied. This is likely due to the disconnected nature of Northern

Hemisphere AR tracks, creating distinct flavors of ARs between those over the Pacific and those over the Atlantic—notice the difference in track orientation, extent, and the more poleward extent of North Atlantic AR terminus locations—and is in stark contrast to the continuous AR track hotspots of the Southern Hemisphere (Figure 3.5a).

Next, we examine the average decadal location of AR frequency, genesis, each averaged over a 5°-by-5° grid (Figure 3.5a-c). We note AR hotspots over 1) the Northern Pacific, which consist of AR counts between 800-900 per decade, with genesis hotspots over southeast China and the northwest Pacific and terminus points over the Pacific coastline from California to the Aleutian Islands; 2) the northern Atlantic, with the greatest number of decadal ARs—greater than 1,000—with genesis over the Eastern U.S. and Northwestern Atlantic and terminus over Northern and Western Europe along with the adjacent parts of the Atlantic; and 3) Southern Hemisphere ARs, which exist continuously across the pathway of the Southern Jet Stream, but show hotspots on both sides of South Africa and west of Chile. Notable genesis hotpots for these ARs include the region of the South American Low-Level Jet (Montini et al. 2019) and southeast of South Africa, with as many as 50 geneses per decade, while there are notable terminus hotpots south of South Africa, in the southern Indian Ocean, and offshore of Chile.

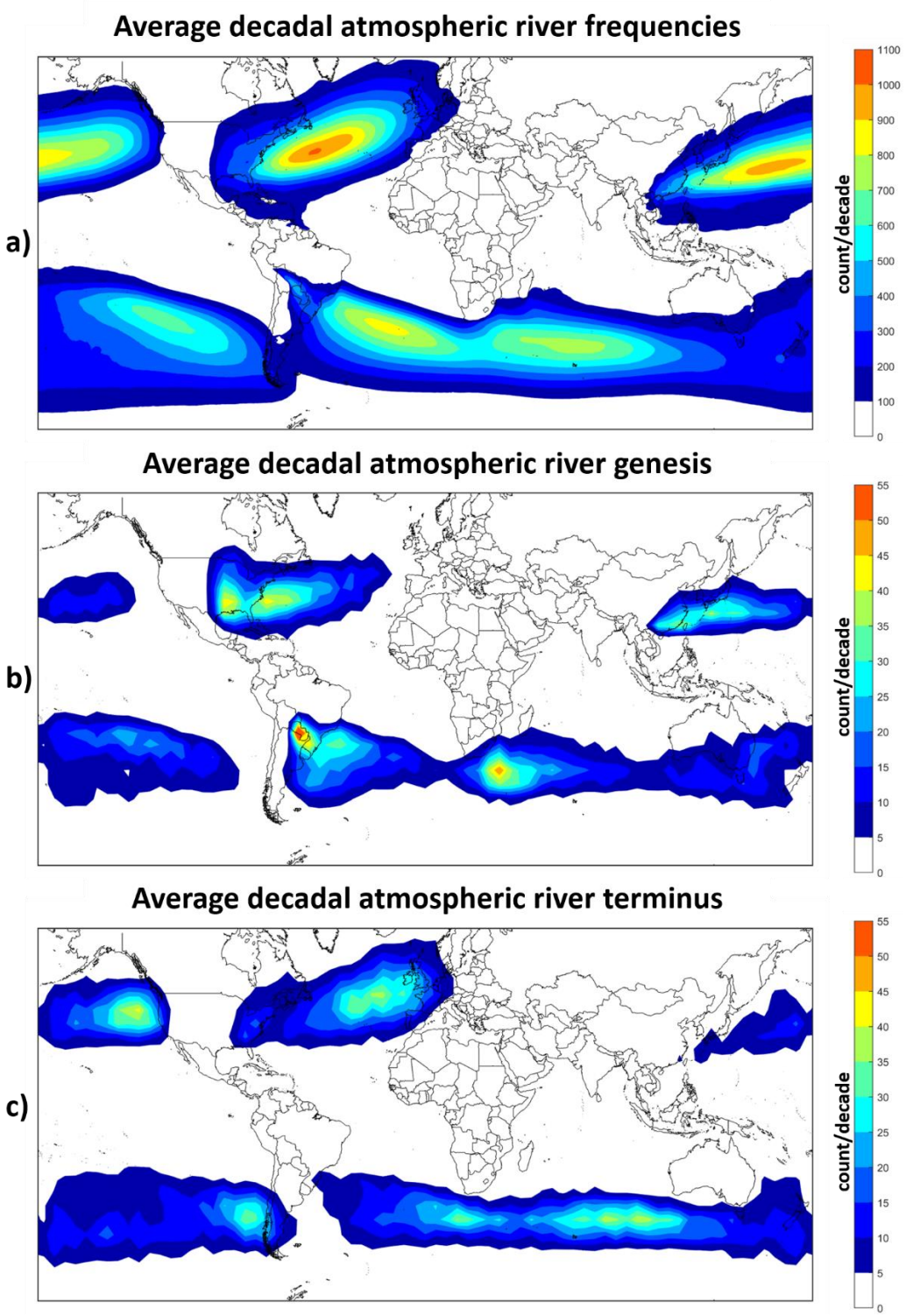

Figure 3-5. (a) The annual climatology of atmospheric river (AR) objects, and the decadal climatologies of (b) AR genesis and (c) AR terminus locations, resampled to a 5°-by-5° grid. Note the clear relationships between the three plots, demonstrating five notable hotspots: two in the Northern Hemisphere and three in the Southern Hemisphere, the latter of which are notably less distinguishable from each other.

3.4.2. Trend Analysis

To understand how AR lifecycles have changed over our 34-year (1983–2016) catalog, we analyze the trends in the timeseries of lifecycle characteristics using slope/pValue (short for "probability value", a term that describes statistical significance) charts. As the sensitivity of these trends during different periods of observation is high owing to the shorter-term domain of the catalog, we examine the trends across every multi-year period possible during the study duration, for a total of 561 trend analyses per variable (Figure 3.6). In this way, clusters of high values are clearly visible and periods of enhancing or decreasing activity can be intuitively digested. Each slope/pValue plot is divided into two halves: 1) the slope of the trend and (bottom-right) 2) the pValue of the trend (top-left). Statistical significance is examined at pValue = 0.10, 0.05, and 0.01.

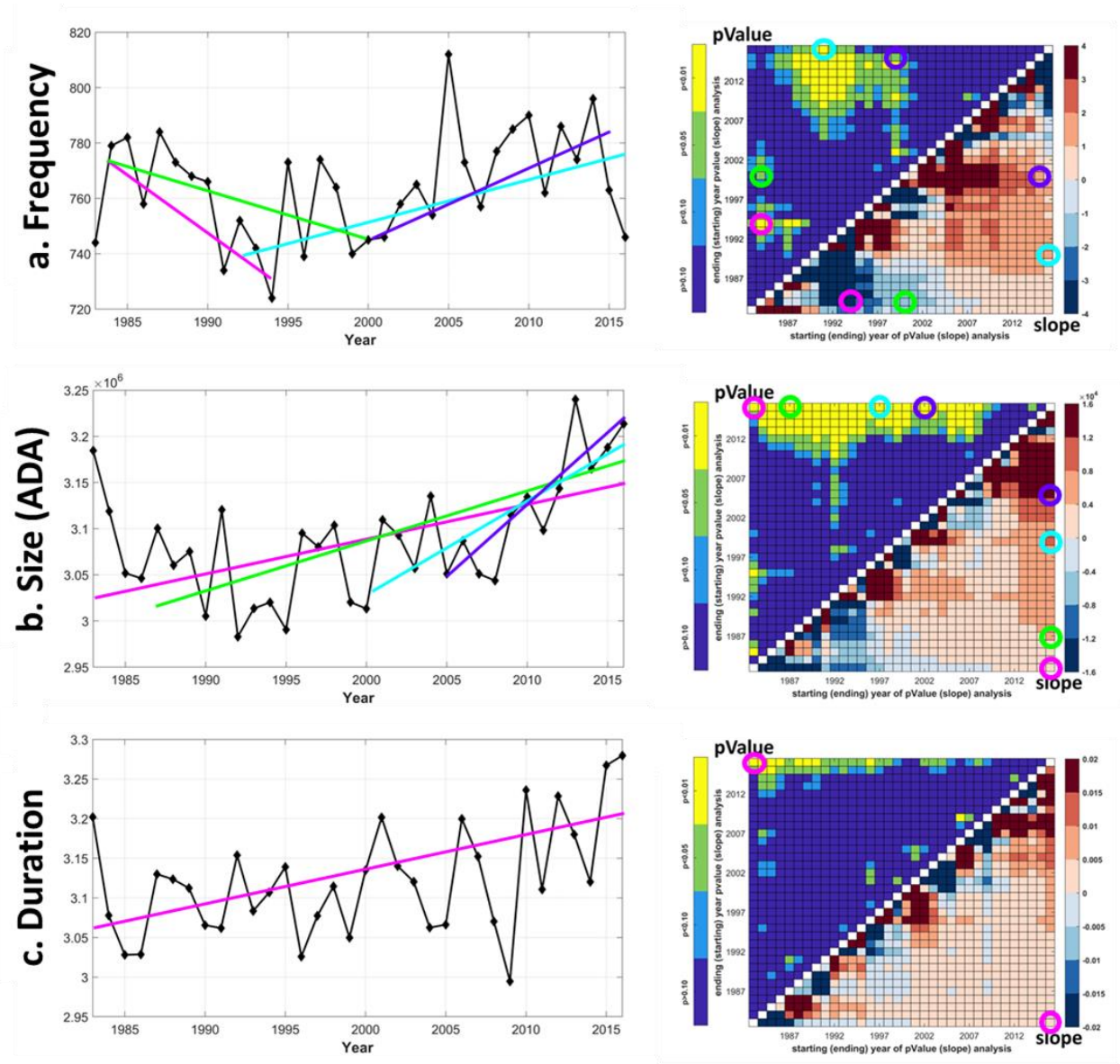

Figure 3-6. Left: Annual averages of atmospheric river (AR) (a) frequency, (b) size (average discrete area), (c) and duration over the study period. Trends are presented as colored lines and correspond to the colored circles signifying slope and significance on the right-hand subfigure. Right: Trends in AR characteristics presented by slope and significance level (pValue) of the trend. Points of trendline slope and pValue for identical time-periods are mirrored across the diagonal line of white grid-points. The greatest duration (1983–2016) subperiods can be observed in the top-left and bottom-right corners of the boxes for the pValue and slope, respectively. Each step left (right) of this point is a 1-year decrease in the ending year for the slope (pValue) time series, and each step up (down) of this point is a 1-year increase in the starting year for the slope (pValue) time series.

The frequency (Figure 3.6a) of ARs per year shows a cluster of increasing AR values of slope between

2-4 ARs/year occurring between approximately 1985 and 2000 to approximately between 2005 and

2016. Another cluster of negatively trending values at a rate between 3-4 ARs/year exists between 1983 and 1989 to between 1991 and 1997. This suggests the possibility of a multi-decadal oscillation in the number of AR appearances per year. When collectively considering the trend between 1984 to 2000 (green) followed by the trend from 2000 to 2015 (purple), we see a near-perfect oscillation: -2 ARs/year in the falling limb followed by a 2 AR/year increase in the rising limb, both significant at a pValue=0.05. The trend of average area (Figure 3.6b) shows a patch of statically significant and strongly increasing trends over longer (10-year+) time periods that end in the last 6-8 years of the record. Such a pattern indicates a strong positive signature in the IVT field, which is the result of anthropogenic heating creating a greater water vapor background climatology, translating into larger plumes of IVT above the 300 kg m^{-1} s^{-1} threshold (Espinoza et al. 2018). For the duration time series (Figures 3.6c), only trends that end over the last two years of the study period show robustness when changing the beginning year. Even when considering the strongest trends, a total increase of only <0.20 days is observed, which is approximately equivalent to 4.5 hours. Overall, the multi-subperiod analysis presented in this study effectively makes diagnosing long-term trends from noise or decadal-scale oscillations visually intuitive. Due to the shorter period of the analysis, there are still considerable questions regarding long-term trends, especially those influenced by anthropogenic climate change. Extending the time series into the past and future via longer duration time series and model projections would give further insight into the trends of annual AR frequency, duration, and size and is a promising direction for AR lifecycle research.

3.4.3. Rainfall

We plot the pattern of quasi-global (60°N–60°S) annual AR rainfall climatology in Figure 3.7 and confirm the presence of sizable amounts of rainfall from landfalling ARs over regions frequently associated with AR activity such as the Western U.S.; Chile; Europe, especially the British Isles; and Oceania. Furthermore, it is shown that regions associated with AR genesis, e.g. central South America,

the eastern U.S., and eastern Asia, have a sizable portion of their rainfall climatologies from AR rainfall, with values up to 50%, though these totals (especially over the eastern United States) are likely exaggerated owing to the higher background moisture fields in these regions, which makes inadvertent capturing of convective systems in AR-CONNECT object boundaries likely.

In terms of validation, we examine that the precipitation fractions over the U.S. West Coast generally fall between 5–30% (Figure 3.7b), which is on the lower end to less than the 18–50% number given by Dettinger (2011), Rutz et al. (2014), and Guan and Waliser (2015). This is expected, as the IVT threshold used in this analysis is greater than the 250 kg m^{-1} s^{-1} threshold typically used over the U.S. West Coast. Furthermore, these studies were done using daily precipitation products, while AR-CONNECT only accumulates precipitation totals during 3-hour increments of AR activity, a more conservative approach. Lastly, the numbers from Dettinger and Rutz are only calculated for the cool season.

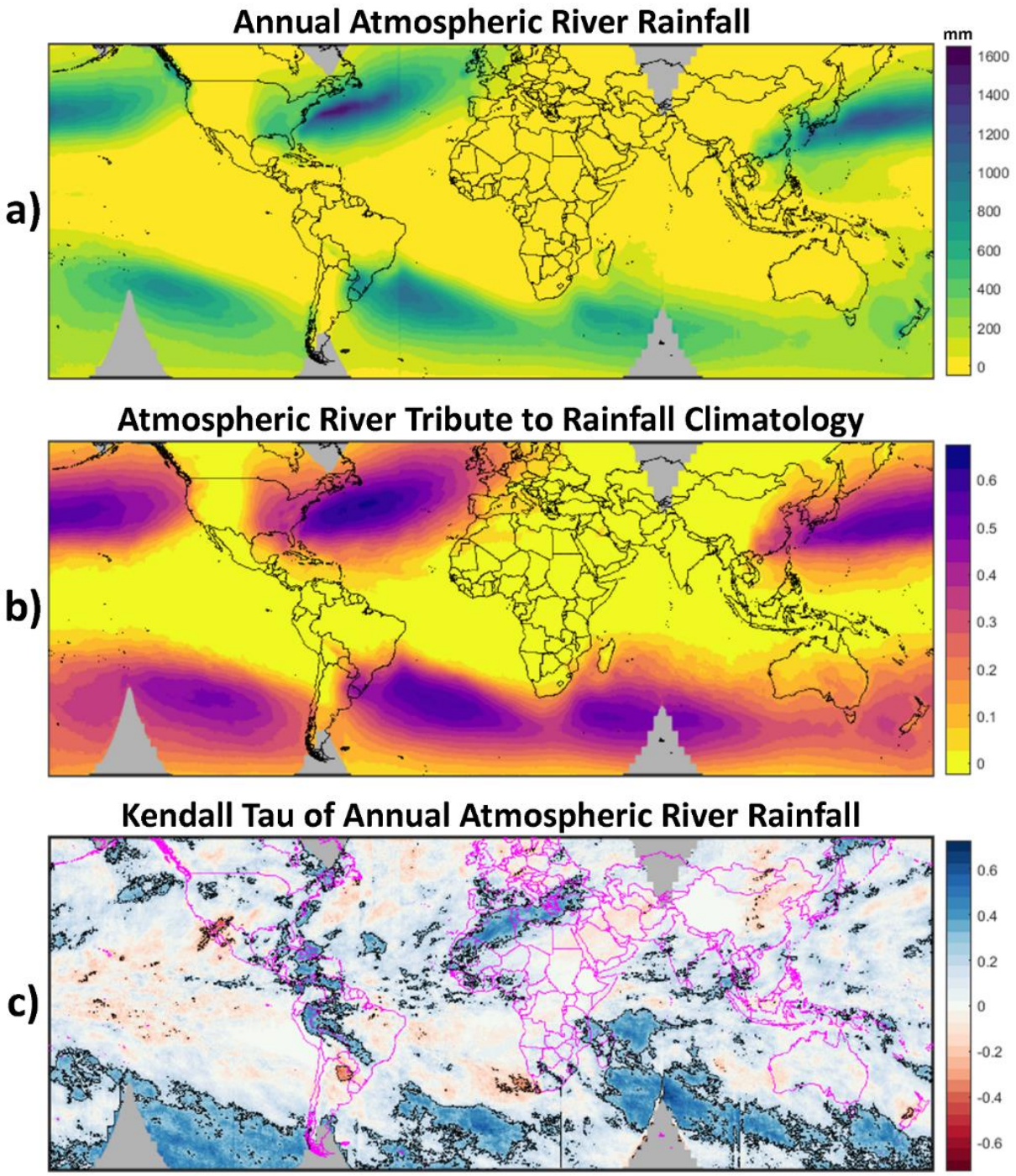

Figure 3-7. Global AR rainfall patterns and trends uncovered by AR-CONNECT and PERSIANN-CDR. Areas in gray are regions where data availability of three-hourly PERSIANN-CDR is <90% of time steps. (a) Average annual AR rainfall measured by PERSIANN-CDR. (b) Average annual AR precipitation (a) divided by annual rainfall climatology measured by PERSIANN-CDR. (c) Results of the Mann-Kendall test done at a significance level $\alpha = 0.05$. Values of Kendall's rank correlation coefficient (tau) are visualized by the red-white-blue color map, with regions of statistical significance indicated with a black outline.

Based on these results, we determine that the AR-CONNECT method shows suitability for identifying regions of frequent AR activity and getting approximate AR rainfall totals and contributions to regional and global rainfall climatologies. For example, AR rainfall totals over Europe show contributions as great as 35% over coastal Ireland and contributions of at least 5% as far northeast as Russia and southeast as Iran. However, it is known that satellite measurements are less accurate than those from radar and rain gauges. Therefore, AR rainfall fractions presented in this study outside of well-studied regions like the west coast of North America need to be reinforced by other global and regional studies.

In terms of AR rainfall trends, trends in annual pixel rainfall totals are analyzed through the Mann-Kendall test at a significance level of α=0.05 and the Kendall rank correlation coefficient (Figure 3.7c). We choose to use Kendall rank correlation, a trend analysis method closely related to the Mann-Kendall test, because it is not affected by missing data, which is an issue with the incomplete coverage of the satellite record back to 1983. Kendall rank correlation ($\boldsymbol{\tau}$) is calculated thusly:

$$\tau = \frac{\sum_{i=1}^{n-1} \sum_{j=i+1}^{n} sgn(x_j - x_i)}{\frac{n(n-1)}{2}}$$

where x is a single value from a vector of annual point rainfall values x and n is the population size of x. In essence, τ is the number of concordant pairs subtracted by the number of discordant pairs divided by the total number of pairwise comparisons, with [1 -1] being the bounds of a perfectly increasing/decreasing time series.

Overall, when considering regions where there is satellite coverage ≥90% of the PERSIANN-CDR data files, annual AR-related rainfall is increasing over 74% of the world's surface, with 17% showing a significant trend. Regions of significantly enhanced rainfall include along the Southern Jet Stream, east of the Andes, and southern Europe to western Asia. The Sahara Desert also shows a significant

positive trend. However, this region is one of the most problematic for remotely sensed quantitative precipitation estimation (Kelley 2014) and should be considered with great scrutiny. Inversely, 23% of the world is seeing a decrease in AR rainfall, though <1% is statistically significant. Regions, where AR rainfall is decreasing significantly include northern Mexico/the American Southwest, New Zealand, and northeastern Argentina, the most latter of which is the hottest spot of AR genesis (Figure 3.5b). Globally, there is a detected positive trend in precipitation volume from ARs significant at α=0.01, contributing 17% of total global rainfall in 1992 to 21% in 2016.

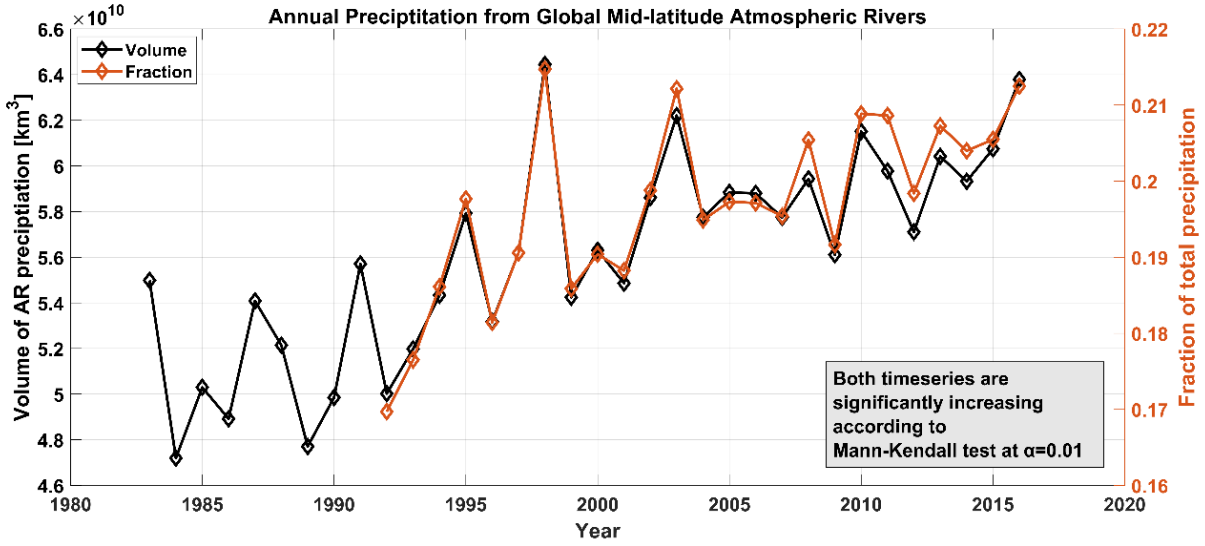

Figure 3-8. Trendlines of precipitation volume by volume (black) and fraction of total quasi-global (60°N-60°S) rainfall (orange). Both trends are significantly increasing at α=0.01 when tested with the Mann-Kendall test. Fraction time series starts in 1992 as holes in the satellite record artificially inflate values before this year.

3.5. Conclusions

In this study, the CONNECT algorithm is adapted to track the lifecycles of global mid-latitude ARs and associated precipitation. This is done by tracking AR "cores", which is shown to be an effective way of extracting singular ARs lifecycles by reducing the existence of conglomerate objects. Furthermore, the new methodology allows AR-CONNECT to track AR geneses back to before they

obtain AR geometries. Despite not having hard-coded geometric requirements to classify an IVT patch as an AR, analysis into the lengths and shape of AR-CONNECT objects show that in general, objects show suitable elongation during their lifecycles to be considered ARs.

Through the AR-CONNECT methodology, we investigate the climatology and trends of AR characteristics such as frequency, size, duration, and centroid location. Generally, the number of ARs lifecycles exists in a 2:3 ratio of Northern Hemisphere to Southern Hemisphere ARs, which is identical to the ratio of AR track hotspots in each hemisphere. Trend analysis indicates that there is a large statistically significant increase in the size and duration of ARs, while there is evidence of an oscillating nature in annual AR numbers coupled with a small increasing trend. The Mann-Kendall test located areas of significantly changing AR rainfall and found that 17% of the world between 60°N–60°S is experiencing a statistically significant increase.

Chapter 4 – Four Decades of Intensifying Precipitation from Tropical Cyclones

4.1. Introduction

One of the barriers to making a conclusive assessment of historic TC precipitation is the lack of high-resolution and global precipitation data available for durations long enough to overcome natural climate variability. Thanks to the rapid advancement of satellite precipitation estimating algorithms, the first HRPCDRs are being produced, making precipitation measurements at 0.04° (~4 km) and sub-daily spatiotemporal resolution available back to 1980. Available at higher resolutions than other long duration records of precipitation like PERSIANN-CDR and Climate Hazards Group InfraRed Precipitation with Station data (CHIRPS), HRPCDRs are shown to better capture the pattern and intensity of the most intense precipitation rates (Sadeghi et al. 2021b)—an invaluable improvement to accurately assess TC precipitation.

In this study, a statistical analysis technique known as object-oriented analysis is used to data mine TC precipitation from an HRPCDR produced from the PDIR model over the 1980-2019 period. Precipitation measurements within 500 km of TC track data are captured and used to calculate characteristics that describe the event's hydrometeorological characteristics, namely the mean, 90th, and 99th percentile of precipitation rates, along with the total volume of precipitation and its component over land. The method of using characteristics to describe an event or "object" is known as object-oriented analysis. Characteristics are considered at an annual basis (calendar year) and are calculated per TC basin determined by genesis location: East Pacific (EP), North Atlantic (NA), North Indian (NI), South Indian (SI), South Pacific (SP), and West Pacific (WP), and together as a global aggregate. Trends are further divided into intensity categories based on their peak windfall

measurements according to the Saffir-Simpson scale (Knapp et al. 2010): "All TCs" constitute all events, "Weak TCs" are all sub-hurricane strength storms, "Strong TCs" include category 1-2 hurricanes, and "Very Strong TCs" indicate any storm at or above category 3 (Figure 4.3). These results paint a varied history in the last 40 years of TC activity, with notable increases in TC precipitation rates across basins and mixed but generally positive changes in total and inland precipitation volumes between basins.

4.2. Materials and Methods

4.2.1. PDIR-CDR Precipitation Data

Upon the development of the first HRPCDR, PERSIANN-CCS-CDR (Sadeghi et al., 2021b), it was shown that one of its distinct advantages over PERSIANN-CDR is in recording extreme precipitation. Given the intensity of rainfall and smaller scale of TCs, especially the sharp gradients of the rainfall field found from the core to the outer extent of a TC, it was shown that an HRPCDR could be a more effective tool for producing a climate-scale catalog of TC precipitation than PERSIANN-CDR. For example, PERSIANN-CCS-CDR outperforms PERSIANN-CDR as a QPE method for recording the rainfall of Hurricane Harvey.

For this study, we produce an HRPCDR based on the PDIR satellite precipitation measurement algorithm (Nguyen et al. 2020a,b), hereafter referred to as "PDIR-CDR". PDIR-CDR uses three-hourly and 0.04° spatiotemporal resolution measurements of IR-derived cloud-top temperature from the GridSat-B1 archive, which is a consistent and homogenous remotely sensed data set available near-continuously since 1980. PDIR-CDR's domain, like many other QPE products, is limited to sub-polar regions (60°S-60°N.) In the instance of missing coverage—mostly occurring in the 1980-1982 period and in the Eastern hemisphere—precipitation estimates from the NASA MERRA-2 (Gelaro et al. 2017) reanalysis project is downscaled from its native 0.625° x 0.5° spatial resolution and used to fill

in the gaps. As the spatial resolution of MERRA is coarser than GridSat-B1, some of the finer spatial patterns in the rain field are lost in the final product, but the inclusion of these years was determined to not seriously change the results of this study. Afterwards, the monthly accumulations of precipitation estimates are bias corrected at the monthly scale using GPCP v2.3 monthly gridded gauge data (Adler et al. 2018), following the homogeneity-focused methodology of other PERSIANN-based CDRs. Though experimental in nature, continued evaluation of PDIR-Now shows generally skillful performance across temporal and spatial scales (Saemian et al. 2021; Huang et al. 2021).

One of the most prominent concerns when producing and utilizing high-resolution data sets of precipitation is their uncertainty. Uncertainty is an unavoidable issue when dealing with satellite remote sensing of precipitation at all scales, or any other hydrological variables for that matter. Even the best multi-input and gauge corrected data sets have considerable issues with accuracy when compared to quality-controlled radar and gauge products (Nguyen et al. 2018a, 2019). This issue is complicated by the fact that there is no perfect 'ground truth' data set to compare most products to as the climate is not regularly and directly measured except at a handful of *in situ* sites (Daly 2006). This is especially true in remote regions or over large bodies of water, where satellite and reanalysis are the only options. To address PDIR-CDR's uncertainty for measuring TC-linked precipitation, we evaluate PDIR-CDR against GPCP v2.3 in the tropics (30°N to 30°S), which shows PDIR-CDR's strong correlation with GPCP (CORR=0.67), though not without notable overestimation bias (Figure 4.1). Though with notable bias and periods of disagreement with GPCP, primarily in the early record (1980-1984), PDIR-CDR does not show the presence of long-term artificial trends that would indicate inhomogeneity, meaning its weaknesses should not dominate trend analysis results as error is distributed quasi-uniformly across the study period. Moreover, robust regression techniques (summarized later in this section) were used to limit the influence of outliers, including periods of disagreement between PDIR-CDR and GPCP. Overestimation bias is expected from PDIR-CDR because the PDIR algorithm was

developed with extreme events in mind, which are frequently underestimated by other QPE techniques (Nguyen et al., 2020a,b). PDIR can better capture the upper tail of extreme rainfall at the cost of frequent overestimation. Moreover, the difference in native resolutions between GPCP (2.5°, monthly) and PDIR-CDR (0.04°, 3-hourly) means that short-duration heavy rain events that are captured in PDIR-CDR are smoothed over in GPCP. PDIR-CDR's high correlation with GPCP is far superior to Tropical Rainfall Measuring Mission (TRMM) Multi-satellite Precipitation Analysis-3B42 v7 (TMPA-3B42 v7; CORR=0.02), though TRMM shows essentially no bias at the monthly scale.

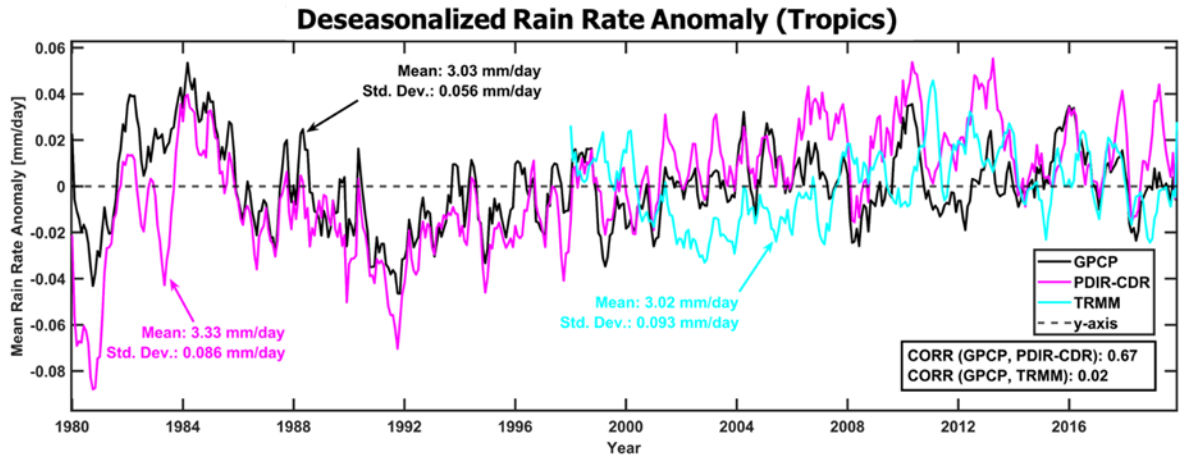

Figure 4-1. Deseasonalized rain anomalies over the tropics (30°N to 30°S) from GPCP v2.3 (black), PDIR-CDR (magenta), and TRMM TMPA-34BT v7 (cyan), measured at the monthly scale. Each data set is described by its mean value and standard deviation over the domain in the colored arrows. Correlations between PDIR-CDR and TRMM with GPCP are reported in the bottom right box.

Further analysis of PDIR-CDR performance and uncertainty was done for select case studies to prove its effectiveness for the capture of extreme precipitation, especially over land. In Figure 4.2 daily rainfall totals from PDIR-CDR over land are evaluated in comparison to NOAA's Stage IV radar-gauge product, a high quality QPE product frequently used for evaluation purposes, during two noteworthy hurricanes that made landfall over large population centers in the United States during the last two decades: Hurricane Katrina (2005) and Hurricane Sandy (2012). By observing the scatter plots

of PDIR-CDR and Stage IV comparisons, we see that though there exists a large amount of noise and bands of notable overestimation and underestimation by PDIR-CDR for Hurricane Katrina and Sandy, respectively, the large cluster of points along the perfect correlation line at the extreme end of the chart (>100 mm/day) show that PDIR-CDR's quality does not decay for large extreme precipitation totals, an important requirement for this study. For both evaluations, PDIR-CDR's performance recorded by statistical comparison metrics remained similar: Probability of detection (POD) of or greater than 0.90, false alarm ratio (FAR) of less than 0.30, cumulating into a combined skill index (CSI) score of ~0.7, an impressive score when considering satellite QPE at the daily scale. PDIR-CDR's multiplicative bias of 0.68 and 0.94 combined with notable root mean squared error (RMSE) scores of 12 mm/day and 13.9 mm/day indicate that even with its overestimation at the monthly scale, PDIR-CDR still underestimates the heavy precipitation rates of heavily precipitating TCs to some degree. FAR scores of 0.20 and 0.29 mean PDIR-CDR occasionally records rainfall where there is none. Compare these results to those from Omranian et al. (2018), who found similar performances (CSI of ~0.7 and correlation of ~0.6) during Hurricane Harvey using what is widely regarded as one of those most accurate satellite remote sensing products, IMERG. Though it's clear that PDIR-CDR is not the perfect dataset, its high CSI score combined with its notable skill for capturing extreme precipitation totals means its well suited for this study.

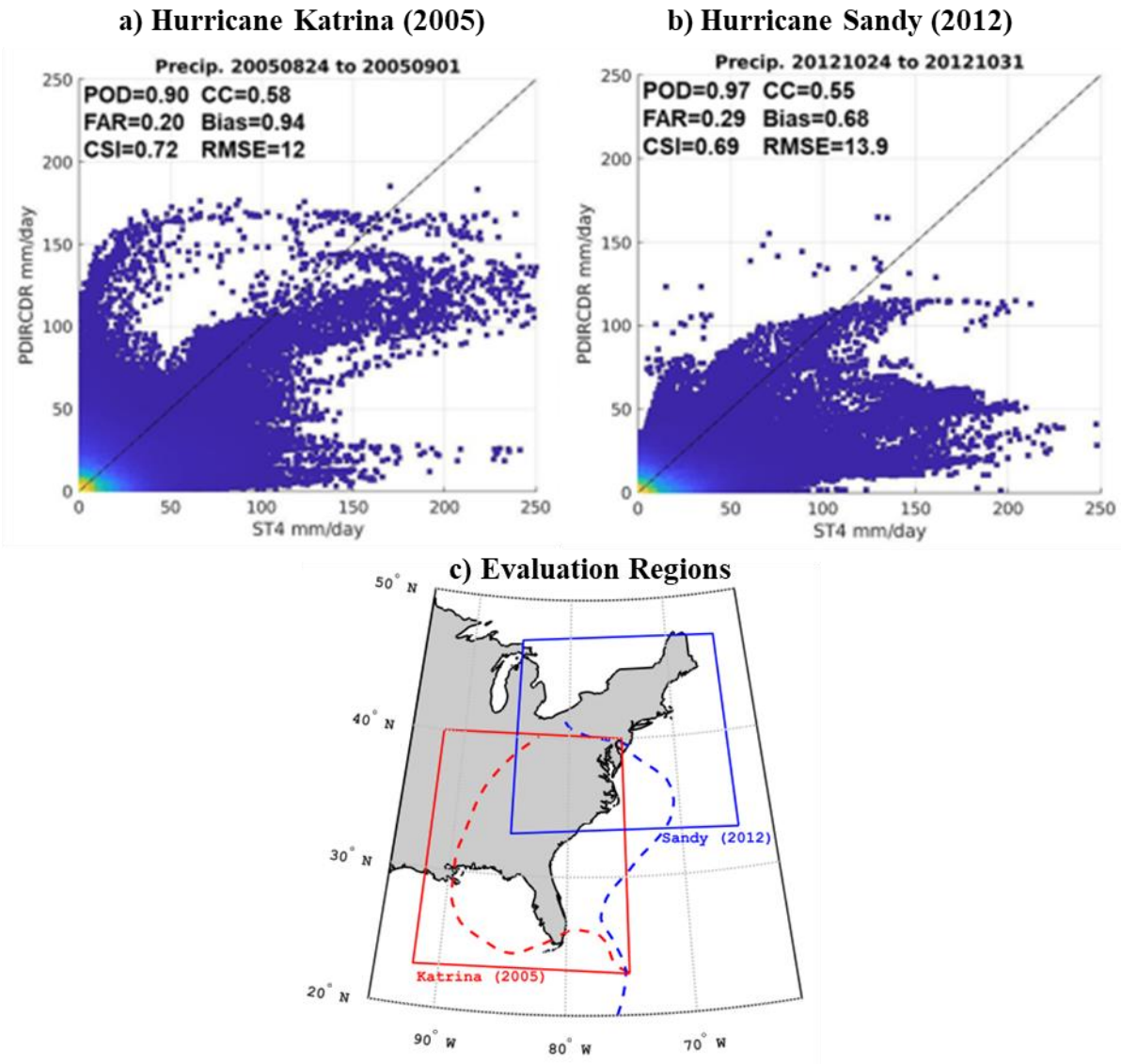

Figure 4-2. Evaluation of PDIR-CDR rainfall data against Stage IV (ST4) radar-gauge data for a) Hurricane Katrina from Aug-24-2005 to Sep-01-2005 and b) Hurricane Sandy from Oct-24-2012 to Oct-31-2012. Scatter plots of daily pixel totals are shown with Probability of Detection (POD), False Alarm Ratio (FAR), Critical Success Index (CSI), Pearson Correlation Coefficient (CC), Multiplicative Bias, and Root Mean Squared Error (RMSE) scores superimposed. The scatterplot's color map represents the density of points, with the greatest density at the origin point in yellow. c) The spatial domain (solid line) of each scatter plot with the corresponding hurricane track (dashed line). Hurricane Sandy is shown in blue while Hurricane Katrina is shown in red.

4.2.2. Tropical Cyclone Segmentation

We use the International Best Tracks Archive for Climate Stewardship (IBTrACS; Knapp et al. 2010) reanalysis data set for TC track data. IBTRaCS is a collaborative effort to produce TC tracks using reanalysis techniques from climate monitoring centers across the globe. Data availability is three-

hourly, corresponding to the resolution of PDIR-CDR. IBTrACS data is used for TC track coordinates from 1980 to 2019 across six basins: EP, NA, NI, SI, SP, and WP. Note that the Southern Atlantic basin was omitted due to sparse activity and the Australian basin was split between the SI and SP basins per IBTrACS convention. Additionally, IBTrACS convention grades TC intensity on the Saffir-Simpson scale regardless of basin.

<table>
<tr><th></th><th>1-minute / 10-minute sustained wind speed (km/h)</th><th>NE Pacific & N Atlantic NHC/CPHC</th><th>NW Pacific JTWC</th><th>NW Pacific JMA</th><th>N Indian Ocean IMD</th><th>SW Indian Ocean MF</th><th>Australia & S Pacific BOM/FMS</th></tr>
<tr><td rowspan="5">Weak TC</td><td><59 / <52</td><td rowspan="2">Tropical Depression</td><td rowspan="2">Tropical Depression</td><td rowspan="3">Tropical Depression</td><td>Depression</td><td>Zone of Disturbed Weather</td><td>Tropical Disturbance</td></tr>
<tr><td>61 / 52-54</td><td rowspan="2">Deep Depression</td><td>Tropical Disturbance</td><td>Tropical Depression</td></tr>
<tr><td>63-69 / 56-61</td><td rowspan="3">Tropical Storm</td><td rowspan="3">Tropical Storm</td><td>Tropical Depression</td><td>Tropical low</td></tr>
<tr><td>70-100 / 63-87</td><td>Tropical Storm</td><td>Cyclonic Storm</td><td>Moderate Tropical Storm</td><td>Category 1 Tropical Cyclone</td></tr>
<tr><td>102-117 / 89-102</td><td>Severe Tropical Storm</td><td>Severe Cyclonic Storm</td><td>Severe Tropical Storm</td><td>Category 2 Tropical Cyclone</td></tr>
<tr><td rowspan="4">Strong TC</td><td>119-131 / 104-117</td><td rowspan="2">Category 1 Hurricane</td><td rowspan="5">Typhoon</td><td rowspan="2">Typhoon</td><td rowspan="3">Very Severe Cyclonic Storm</td><td rowspan="3">Tropical Cyclone</td><td rowspan="3">Category 3 Severe Tropical Cyclone</td></tr>
<tr><td>133-152 / 119-133</td></tr>
<tr><td>154-176 / 135-154</td><td>Category 2 Hurricane</td></tr>
<tr><td>178-180 / 156-157</td><td rowspan="2">Category 3 Hurricane</td><td rowspan="2">Very Strong Typhoon</td><td rowspan="3">Extremely Severe Cyclonic Storm</td><td rowspan="3">Intense Tropical Cyclone</td><td>Category 4 Severe Tropical Cyclone</td></tr>
<tr><td>181-207 / 159-181</td></tr>
<tr><td rowspan="3">Very Strong TC</td><td>209-226 / 183-198</td><td rowspan="3">Category 4 Major Hurricane</td><td rowspan="3">Violent Typhoon</td><td rowspan="3">Category 5 Severe Tropical Cyclone</td></tr>
<tr><td>228-239 / 200-209</td><td rowspan="2">Super Typhoon</td><td rowspan="2">Super Cyclonic Storm</td><td rowspan="2">Very Intense Tropical Cyclone</td></tr>
<tr><td>241-252 / 211-220</td></tr>
<tr><td></td><td>>252 / >222</td><td>Category 5 Major Hurricane</td><td></td><td></td><td></td><td></td></tr>
</table>

Figure 4-3. The grading scale used in this paper compared to 1-minute and 10-minute wind speed along with regional meteorological offices' grading categories.

To designate rainfall as linked to a TC event, a 500-kilometer buffer is drawn around each IBTrACS centroid location: all rainfall within this buffer is recorded as TC rainfall while all remaining rainfall pixels are ignored. The 500-kilometer radius of TC rainfall is based on the physical structure of a fully formed TC and contains the entirety of the precipitation fields for 90% of TC events (Prat and Nelson 2013; Larson et al. 2005; Lau et al. 2008; Jiang and Zipser 2010; Schreck and Molinari 2011). It should be stated that assuming a perfect circular threshold with a static threshold is a considerable oversimplification of TC structure, which frequently occur in oblong shapes—especially before cyclogenesis—at spatial scales that drastically differ between storms with otherwise similar intensities

(Chavas and Emanuel 2010). However, without readily available data on the radius of the outermost closed isobar, a common way to segment the boundary of a TC—calculated systematically in (Weber et al. 2014) but not made publicly available—alternative methods are questionably better than our simplified approach. For example, (Skok et al. 2013) uses an object-based approach but fails to detect precipitation in 12% of global TC events. Likewise, the outmost radius of 34-kt winds provided by IBTrACS, another metrics useful for calculating the TC size is not available for all basins (e.g. NI, EP) and is significantly less than true TC size (2009). For these reasons, the simplified approach of the 500-km buffer is preferred for this study, though will result in overestimation bias in the results due to detection of non-TC precipitation signatures (Feldmann et al. 2019).

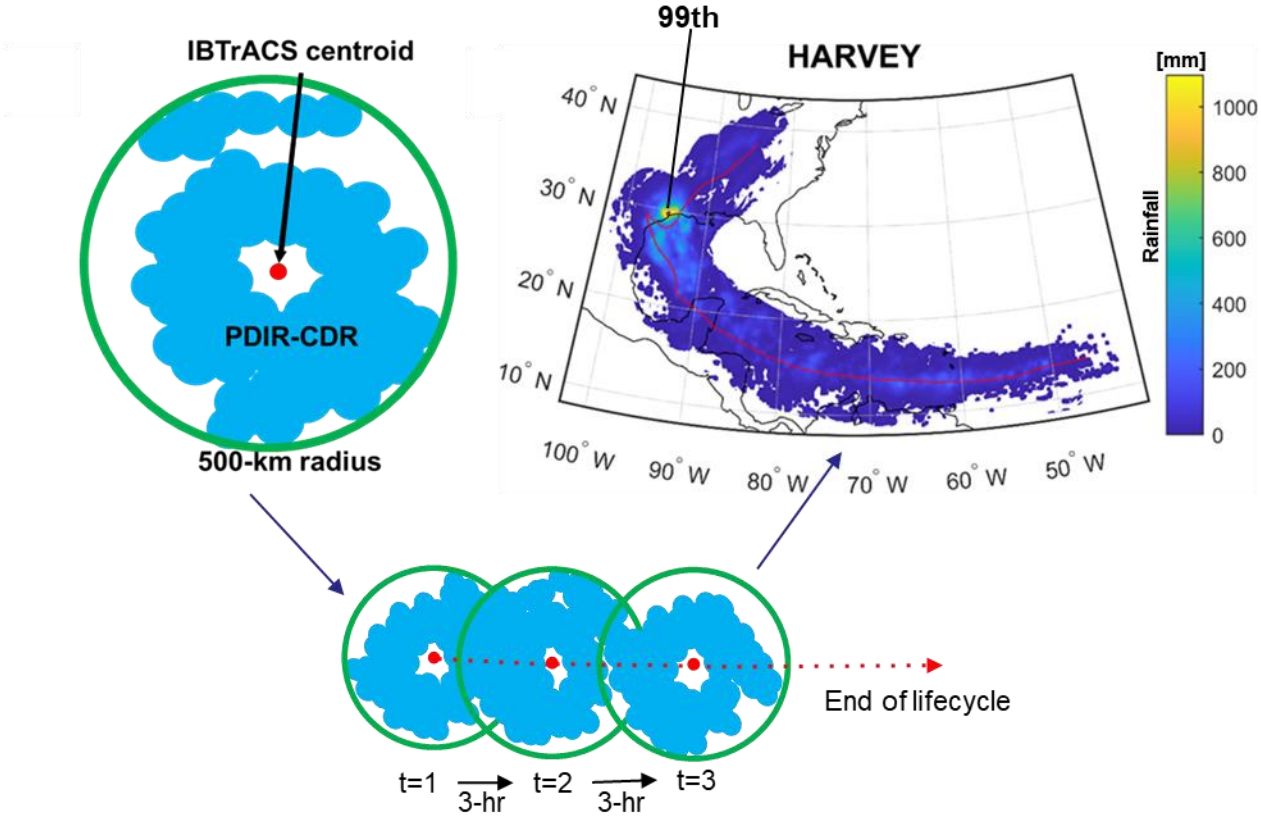

Figure 4-4. Segmentation technique used to classify precipitation as tropical cyclone related.

4.2.3. Trend Analysis Tests

As the natural variability of TC characteristics and the uncertainty of rainfall estimates in the early data period are large, trend analysis was calculated using robust regression. M-estimation, a class of extremum estimators, are robust regression techniques that are often used as an alternative to the linear-least squares method due to their decreased sensitivity to outliers and independence from assuming distribution. Robust regression calculations presented in this paper were performed using MATLAB's "robustfit" function that is based on the iteratively reweighted least squares M-estimation method (Dumouchel 1992). Reductions in degrees of freedom caused by five-year smoothing were considered during trend analysis calculations. All robust regression calculations were tested against a p-value=0.05.

The Mann-Kendall test is a non-parametric trend analysis test that analyzes data collected over time for monotonic (consistently increasing or decreasing) trends. The Mann-Kendall test's non-parametric nature means its suitable for use when data points are missing, making it useful for time series with missing data points, e.g. for analysis of basins with years without precipitation. Based on the Mann-Kendall test, the Kendall rank correlation (τ) is a normalized trend analysis metric with bounds [1 -1] corresponding to a perfectly increasing/decreasing time series. See Section 3.4.3 for more information.

4.2.4. Continuous and Categorical Skill Metrics

The performance of PDIR-CDR was evaluated by the following continuous skill metrics: Pearson correlation coefficient (CORR), multiplicative bias (BIAS), and root-mean-square error (RMSE)

$$CORR = \frac{1}{n} \frac{\sum_{i=1}^{n}(P_i - \bar{P})(O_i - \bar{O})}{\sqrt{\sum_{i=1}^{n}(P_i - \bar{P})^2} \sqrt{\sum_{i=1}^{n}(O_i - \bar{O})^2}}$$

$$BIAS = \frac{1}{n} \sum_{i=1}^{n} \frac{P_i}{O_i}$$

$$RMSE = \sqrt{\frac{1}{n}\sum_{i=1}^{n}(P_i - O_i)}$$

where P_i and O_i represent the i^{th} precipitation estimate from the model and observation data sets, respectively, and n is the number of data comparisons.

We use also evaluate PDIR-CDR using categorical skill metrics: Probability of Detection (POD), False Alarm Ratio (FAR), and Critical Success Index (CSI)

$$POD = \frac{H}{H + M}$$

$$FAR = \frac{F}{F + H}$$

$$CSI = \frac{H}{H + F + M}$$

where H (hit) indicates that the model and observation dataset agree on the presence of rainfall, M (miss) identifies events detected in observations but missed by the model, and F (false alarm) indicates events detected by the model but not confirmed by observation.

4.3. Results

Recent evidence has suggested that an increase in global TC precipitation rates is detectable in historical rain data archives (Guzman and Jiang 2021), though these studies are limited in spatiotemporal extent. To investigate if these trends exist in the climate scale or are rather the result of natural variability in sub-climate timescales, the mean and extreme values of TC precipitation are considered at a yearly basis over a 40-year period. We ask the question: "When considering the distribution of rainfall rate values, do we observe an increase in the mean consistent with expectations

of Clausius–Clapeyron to super Clausius-Clapeyron scaling—expected in kilometer- and sub-daily scale processes (Fowler et al. 2021)—and do we see an elongation of the tail indicating greater extreme values?" To probe this question, the mean ($\langle R \rangle$), 90th (R_{90}), and 99th (R_{99}) percentile of precipitation rates over the life cycle of a TC (rainy grid cells only) were calculated, organized by basin and intensity classifications, then averaged annually. To overcome the fundamental variability in TC events, values are smoothed over a five-year window and trends were tested using robust linear fitting, which helps limit the influence of outliers. The results of this analysis can be seen in Figure 4.5, where trends in precipitation rates are reported as annual percent changes (APC) measured by the fitted model, and in Figure 4.6 where the vertical intercepts of each model are presented. In general, most regions, categories, and precipitation rates are seeing significantly increasing trends over the study period. These are reflected by significant increases globally across intensity basins (12-18%/40 years), with average APC in $\langle R \rangle$, R_{90}, and R_{99} of 0.32±0.03%/year, 0.42±0.04%/year and 0.41±0.04%/year, respectively, in the All TCs category and between 0.42-0.70%/year (17-28%/40 years) in Strong and Very Strong TCs. However, when considering the "global" category, it is important to note that WP basin has >30% of global TC occurrences of all basins (Table 2) and will inevitably influence trends greater than other basins—for example the NI basin, which includes less than 10% of TC events per year. This influence will also exist in the results presented in Figures 4.7, 4.8, and 4.9.

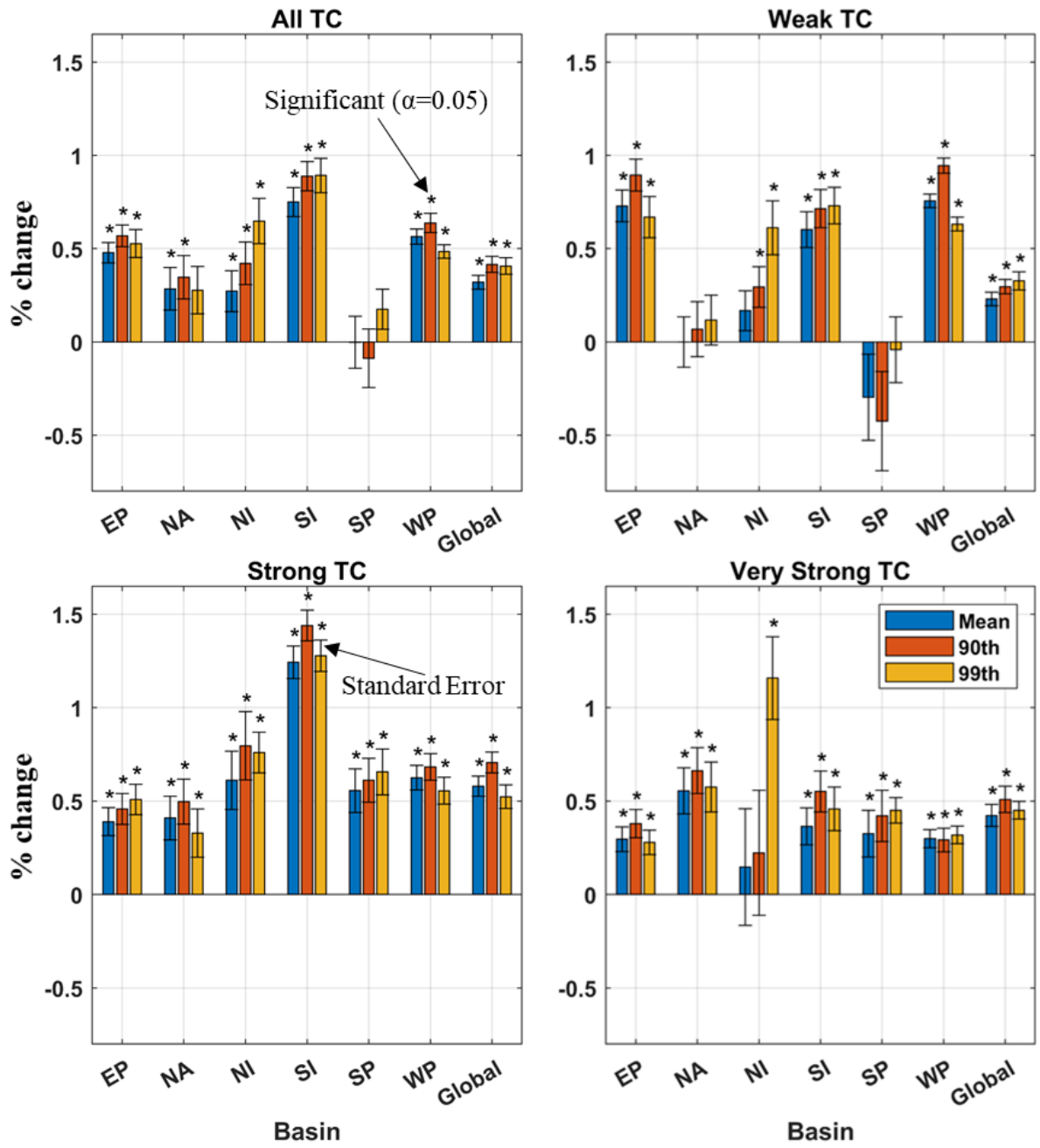

Figure 4-5. Annual precipitation rate changes of mean and upper percentile precipitation rates by intensity classifications and basins— East Pacific (EP), North Atlantic (NA), North Indian (NI), South Indian (SI), South Pacific (SP), and West Pacific (WP). Rates are calculated from the average year-to-year increase of the fitted linear model. Asterisks represent statistical significance at α=0.05. During this period, global mean sea surface temperature increased at a rate of 0.13°C/decade. Knutson et al. (2018) identifies warming in the tropics occurs at ~75% the rate of global temperatures, translating into a ~0.10°C/decade trend in the tropics.

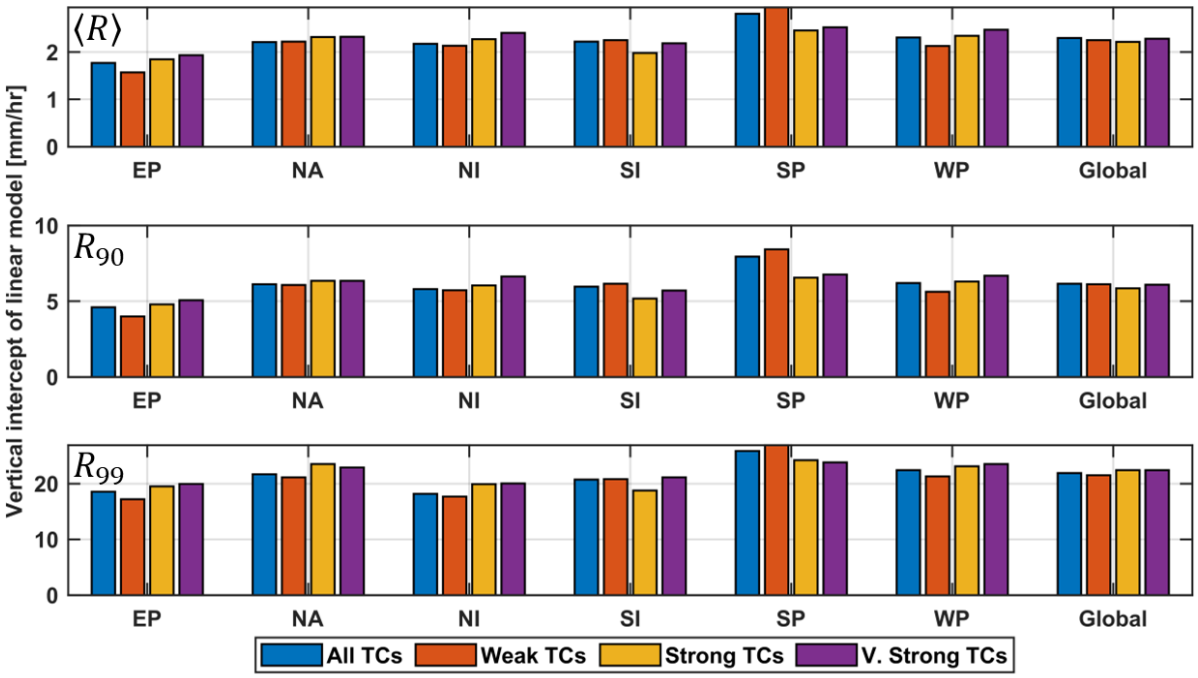

Figure 4-6. The values of the vertical intercepts for the linear models fit in Figure 4.5 for mean rainfall (top), the 90th percentile of rainfall (middle), and the 99th percentile of rainfall (bottom).

Table 4-1. Tropical cyclone (TC) occurrences from 1980-2019 by basin and intensity. Percentages are per intensity classification (i.e. all percentages in the All Tropical Cyclone (ATC) category add to 100%) and the numbers in parenthesis are the totals. WTC, STC, and VSTC stand for Weak, Strong, and Very Strong TCs, respectively.

	EP	NA	NI	SI	SP	WP
ATC	19% (827)	14% (618)	7% (311)	17% (745)	11% (474)	31% (1,340)
WTC	18% (433)	14% (356)	10% (249)	17% (427)	12% (287)	29% (712)
STC	21% (260)	16% (197)	3% (42)	18% (215)	11% (140)	30% (364)
VSTC	21% (134)	10% (65)	3% (20)	17% (108)	8% (54)	41% (265)

Given the consistent increases in precipitation rates, one may assume that that the mean volume of precipitated water per event has also increased. To determine this, TC volume is measured per storm and averaged yearly. TC volumes are calculated by multiplying each rainy grid cell by the grid cell area (latitude-dependent), then summing over the storm's lifetime (see the Methods section for specifics on grid size and TC extent). The time series of mean annual TC precipitation volumes ($\langle V \rangle$, hereafter referred to as "volume(s)") are plotted in Figure 4.7, separated by category and basin. Again, five-year

smoothing was applied to the time series and trends were tested using robust linear fitting. The time series at the top-right of Figure 4.7 provide a summarizing view of global $\langle V \rangle$ trends: increasing at a rate of 0.28±0.10% per year, though not without a strong oscillation in the time series. Indeed, most categories have either seen an increasing trend or no trend, though no basin has seen increasing trends across all intensity categories. Of particular interest are the following results: 1) A sharp increase in volumes in the SI (1.26±0.05%/yr or 48-52%/40-yr) and NA (1.53±0.06%/yr or 59-64%/40-yr) basins driven by Weak and Strong TCs; 2) A modest increase in volumes from Very Strong TCs in the SP basin (APC=0.87±0.18%); and 3) A negative trend in the volumes of Strong and Very Strong TCs in the WP basin of -0.44±0.16% and -0.42±0.12%, respectively, the latter of which has seemingly caused a decrease in global Very Strong TC volumes of 12-20%. Overall, Weak TCs have seen increases in four of six basins, Strong TCs have changed in three of six, with two positive trends and the other negative, and Very Strong TCs have an increasing and decreasing trend in one basin each. This culminates into the All TCs category having increased in three out of six basins.

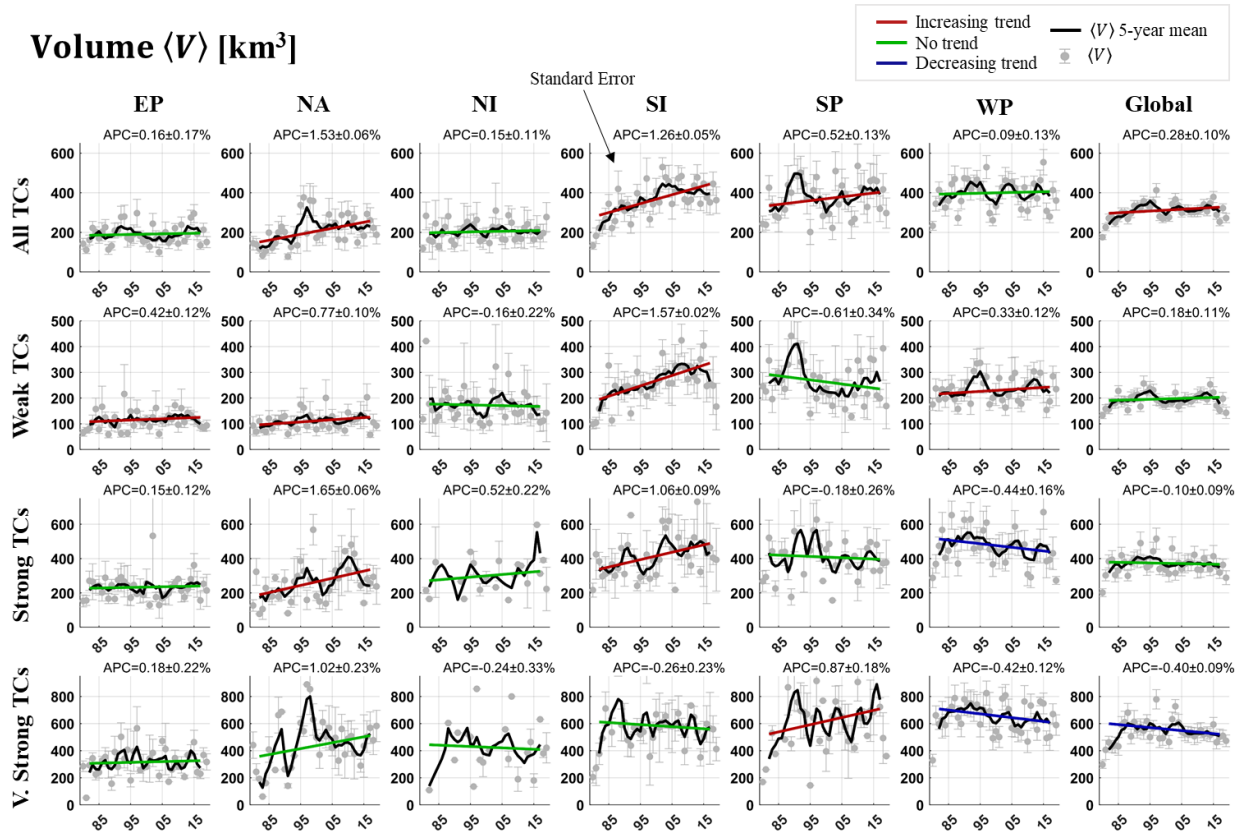

Figure 4-7. Trend analysis of mean TC precipitation volume totals (⟨V⟩), separated by intensity and basin classifications. Gray values with standard error uncertainty bounds indicate annual average values while black lines display five-year average timeseries data. Colored lines indicate trend of the fitted linear model and the colors red, blue, and green indicate a statistically significant increasing, decreasing, and insignificant trend at α=0.05, respectively. Numbers on the top right of each subfigure are the annual percent change (APC) of the trend line and the standard error. Time-axis units are the last two digits of the calendar year, from 1980 to 2019.

Trends in ⟨V⟩ could be interpreted as being a result of increases in TC duration and not necessarily precipitation intensity. Increases in global SST values have been linked to slowing of TC translation speeds (Kossin 2018) and slower decay following landfall (Li and Chakraborty 2020) both increasing TC duration values. We normalize the ⟨V⟩ quantity by its duration in hours to produce hourly ⟨V⟩, hereafter symbolized as ⟨hV⟩. The results of this analysis, shown in Figure 4.8, is that across categories there have only been increasing or non-significant (no) trends. Only one basin/intensity pair has a no trend in ⟨hV⟩ and a positive trend in ⟨V⟩, which indicates an increase in volume from an increase in duration rather than changes in precipitation. All other time series with positive trends in ⟨V⟩ (max:

1.24%±0.06 per year) have also experienced an increase in $\langle hV \rangle$. Simply put, in most cases an increase in TC precipitation volume is at least partially a result of increasing precipitation rates and not solely duration. Increasing trends in Very Strong TC $\langle hV \rangle$ in the global and WP categories hint that the corresponding decreasing trends in $\langle V \rangle$ are a result of a decrease in event duration. Further analysis into TC durations confirms these results, with decreasing trends of -0.56±0.11% and -0.32±0.09% for WP and global Very Strong TC duration, respectively. Other notable negative trends in duration (Table 2) occur in global Strong TCs (-0.51±0.08%/year) and All TCs in the NI (-0.43±0.16%/year) and WP (-0.44±0.12%/year) basins, while increasing trends occur in NA (0.78±0.07%/year) and SI (0.53±0.08%/year). These results are calculated solely from track data. In general, these results are in line with the analysis done in (Lavender and McBride 2021), who found that 70% of variance in the trends of TC precipitation volume during the 1998-2014 period could be explained by changes in TC duration.

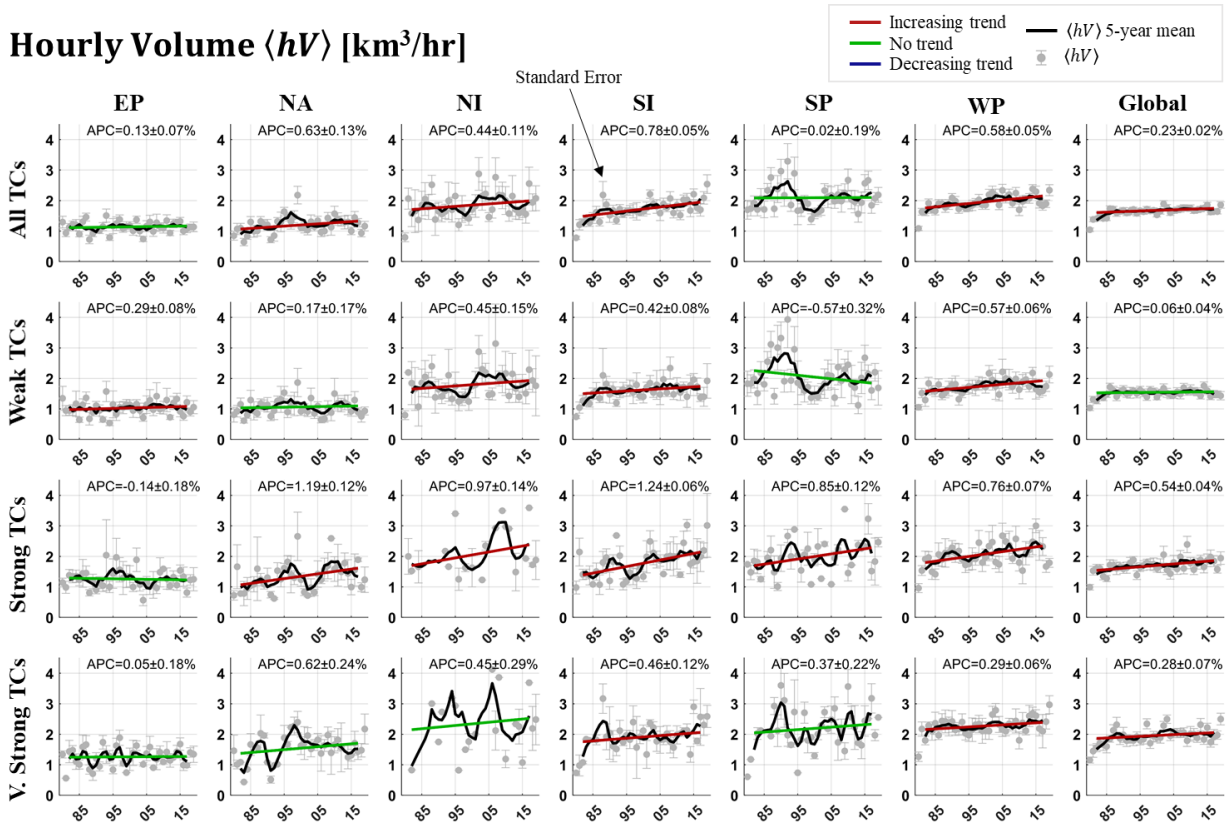

Figure 4-8. Trend analysis of mean hourly TC precipitation volume totals ($\langle hV \rangle$), separated by intensity and basin classifications. The symbology and features are identical to those from Figure 4.7.

Table 4-2. The annual percent change in TC duration over the 1980-2019 period. Bolded numbers indicate statistically significant trends at α=0.05.

	EP	NA	NI	SI	SP	WP	Global
ATC	0.28±0.13%	**0.78±0.07%**	**-0.43±0.16%**	**0.53±0.08%**	0.12±0.14%	**-0.44±0.12%**	-0.00±0.08%
WTC	**0.66±0.08%**	**0.71±0.07%**	**-0.87±0.19%**	**0.86±0.04%**	-0.30±0.19%	-0.29±0.16%	0.02±0.08%
STC	0.30±0.13%	0.21±0.12%	0.03±0.39%	**-0.32±0.07%**	**-0.79±0.33%**	**-1.23±0.14%**	**-0.51±0.08%**
VSTC	0.07±0.16%	0.46±0.20%	-0.03±0.14%	**-0.46±0.16%**	**0.60±0.14%**	**-0.56±0.11%**	**-0.32±0.09%**

Considering the observed increases in rainfall rates and volumes, we now consider if changes are occurring over human population centers, i.e. do we see greater TC precipitation volumes over land? To calculate this metric ($\sum V_{land}$, where *land* indicates the landfalling component of TC volume and the summation sign indicates a yearly accumulation rather than an average), precipitation volumes are decomposed into their fractions over oceans and land and accumulated annually. As can be seen in

Figure 4.9a, increasing trends are the most common of all trends, where they are recorded in 16 out of 28 (57%) basins, while only Weak TCs in the WP and Strong TCs in the SP have seen decreasing trends. Most positive trends can be seen in the Very Strong TC category, where they're recorded in four out of six basins. Global Very Strong TCs have changed at an alarming rate, with a calculated increase of 81-85% over the study period (2.08±0.05%/year). Weak TCs have increased (changed) in three (four) out of six basins, most notably in the NA by 104-106% in 40 years (2.63±0.02%/yr). Overall, these increases are enough for the global trend to be positive (0.30±0.12%/year). Strong TCs are increasing in two basins but aren't enough to produce a significant trend in the global category. Overall, $\sum V_{land}$ in All TCs has increased globally by 24-32% in 40 years (0.70±0.11%/year) and in four out of six basins.

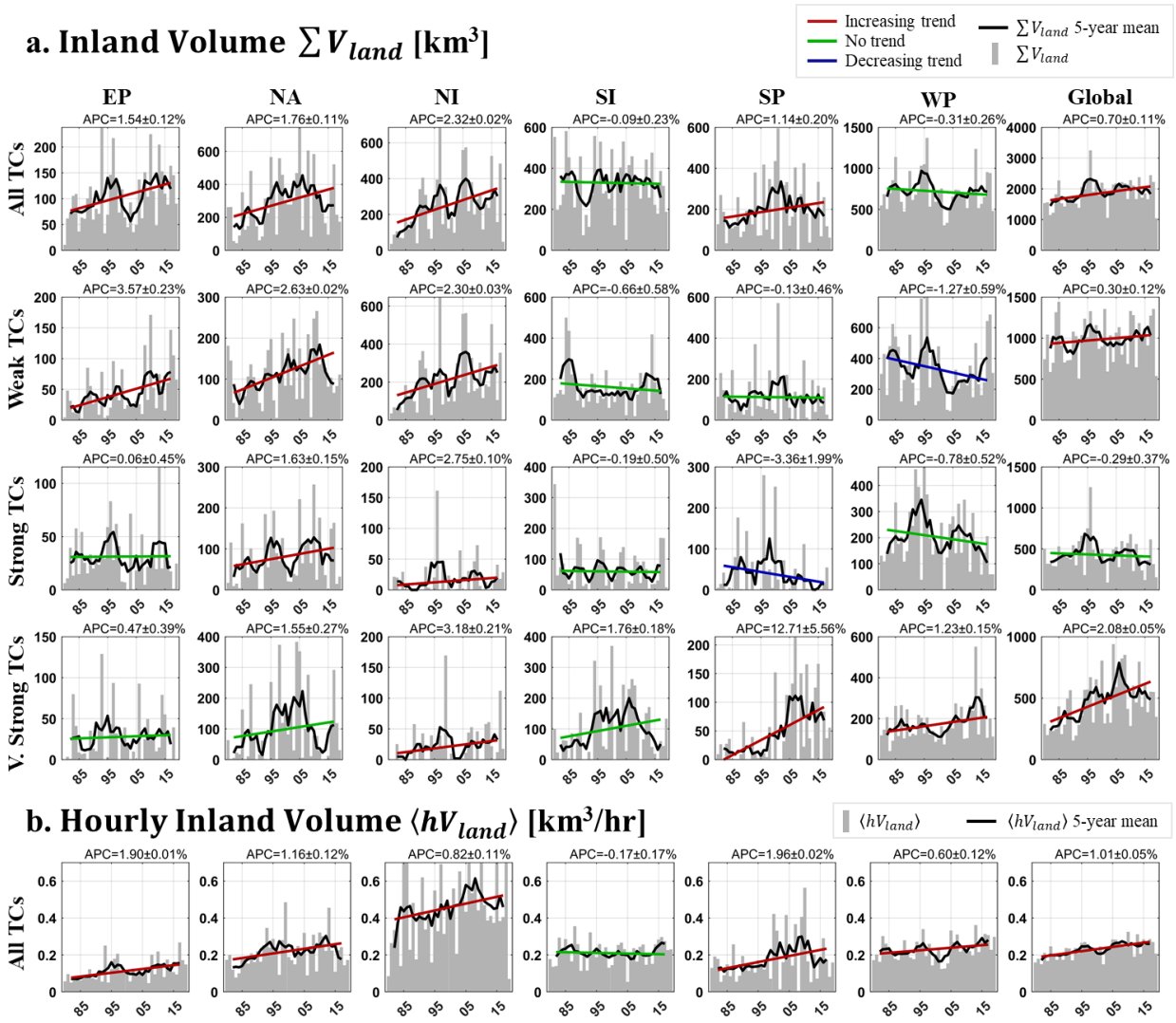

Figure 4-9. Trend analysis of landfalling tropical cyclone (TC) precipitation volume variables, separated by intensity and basin classifications. Symbology is mostly identical to Figures 4.7 and 4.8, except for gray bars indicating one-year accumulations/averages of landfalling TC precipitation. a. Trends in yearly over land tropical cyclone precipitation volume accumulations ($\sum V_{land}$). b. Trends in mean hourly landfalling precipitation volumes ($\sum hV_{land}$), defined as the amount of precipitation an average TC per category drops over land per hour. Note only the All TCs category is shown as values were similar across all intensity categories, making their differences insignificant. Plainly, because $\sum hV_{land}$ from a Weak TC, a Strong TC, and a Very Strong TC are similar, trends are sufficiently represented in the All TCs category.

As values of $\sum V_{land}$ are inevitably linked to the number of landfalling TCs in a year and the duration they remain over land, trends in $\sum V_{land}$ were correlated against those of TC duration over land and landfalling frequency (Table 4, 5). Consistent with expectations, most categories correlate with landfalling frequency at α=0.05: this is true in 20 out of 28 (71%) of the time series and 100% of the

Very Strong TC timeseries. Likewise, $\sum V_{land}$ correlates with duration over land in 17 of 28 (61%) of the time series. Curiously, time series of global All TCs, Weak TCs, and Strong TCs are uncorrelated with TC landfalling frequency.

Table 4-3. Correlation coefficient of $\sum V_{land}$ and annual frequency of landfalling TCs. Bolded numbers indicate statistically significant trends at α=0.05.

	EP	NA	NI	SI	SP	WP	Global
ATC	**0.50**	**0.43**	**0.84**	**0.71**	0.17	**0.44**	-0.06
WTC	**0.76**	0.06	**0.90**	0.29	**0.35**	**0.67**	-0.23
STC	0.20	0.22	**0.67**	**0.73**	**0.58**	**0.38**	0.13
VSTC	**0.61**	**0.87**	**0.68**	**0.82**	**0.48**	**0.57**	**0.73**

Table 4-4. Correlation coefficient of $\sum V_{land}$ and TC duration over land. Bolded numbers indicate statistically significant trends at α=0.05.

	EP	NA	NI	SI	SP	WP	Global
ATC	**0.60**	**0.85**	-0.30	**0.33**	**0.46**	**0.39**	**0.78**
WTC	0.23	**0.67**	-0.04	**0.46**	**0.57**	**0.39**	**0.70**
STC	**0.34**	**0.78**	0.24	0.27	**0.43**	**0.56**	**0.79**
VSTC	0.21	0.25	0.24	0.23	0.27	0.07	**0.74**

To investigate how precipitation intensity over land—independent of frequency and duration—has changed over time, a new variable was calculated: hourly mean precipitation volume over land ($\langle hV_{land} \rangle$), which in essence is $\sum V_{land}$ normalized by its temporal and frequency components. Or it can also be thought of as the over land component of $\langle hV \rangle$. In the simplest terms, it is the average precipitation volume a TC drops over land in one hour. As shown in Figure 4.9b, most basins—as well as the global category—have seen an increase in $\langle hV_{land} \rangle$ over the period, indicating an increase in precipitation volumes over land independent of frequency or duration, except for in the SI basin where $\sum V_{land}$ is also stagnant. Increases are significant, with APC of 1.90±0.01%/year, 1.16±0.12%/year, 1.96±0.02%/year, and 1.01±0.05%/year recorded in the EP, NA, SP, and globally, respectively.

The trends in $\sum V_{land}$ presented in Figure 4.9a can be considered concurrently with Figure 4.10, where trends in $\sum V_{land}$ are tested spatially over major river basins using the Kendall rank correlation metric (useful for basins for years with no activity; see Materials & Methods for more information)—though only for the "All TCs" category. Basins are only considered if over half the years on record include a nonzero value of $\sum V_{land}$, which meant that five-year smoothing could not be used as it was for Figures 4.5-4.9. In summary, every major river watershed recording significant changes are located within the North American continent and the Indian subcontinent and have witnessed increases in $\sum V_{land}$. This helps illustrate the positive trends in $\sum V_{land}$ uncovered in Figure 4.9a for the NA, EP, and NI basins. East Asia and Australia have seen mixed insignificant trends, consistent with the no trend results for the WP and SI basin, though at odds with the increasing trend found for the SP basin. This can be explained by differences in the trend detection tool. For reference, Figure 4.11a and 4.11b shows where TC precipitation is located and its contribution to climatology. Between the insignificant trends detected in Figure 4.10a and the lack of appreciable rainfall from TCs shown in Figure 4.11, the trends in the Arabian Peninsula, East Africa, South America, and the Maritime Continent basins are ignored in this figure and in further discussion.

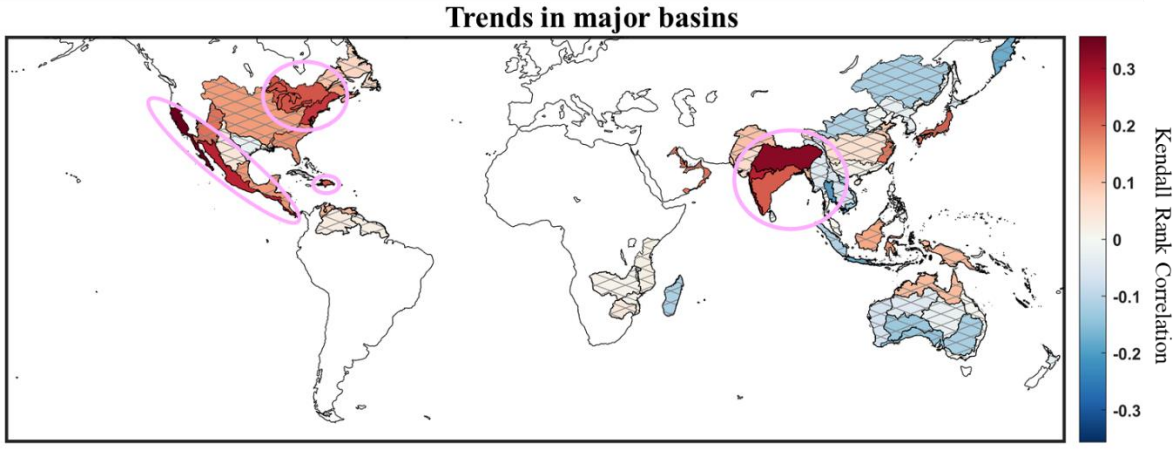

Figure 4-10. Inland precipitation accumulation trends from 1980-2019 calculated at the major river basin scale. Regions of non-significant trends are indicated by gray hatching. Pink circles denote regions where inland penetration from TCs have been heightened significantly.

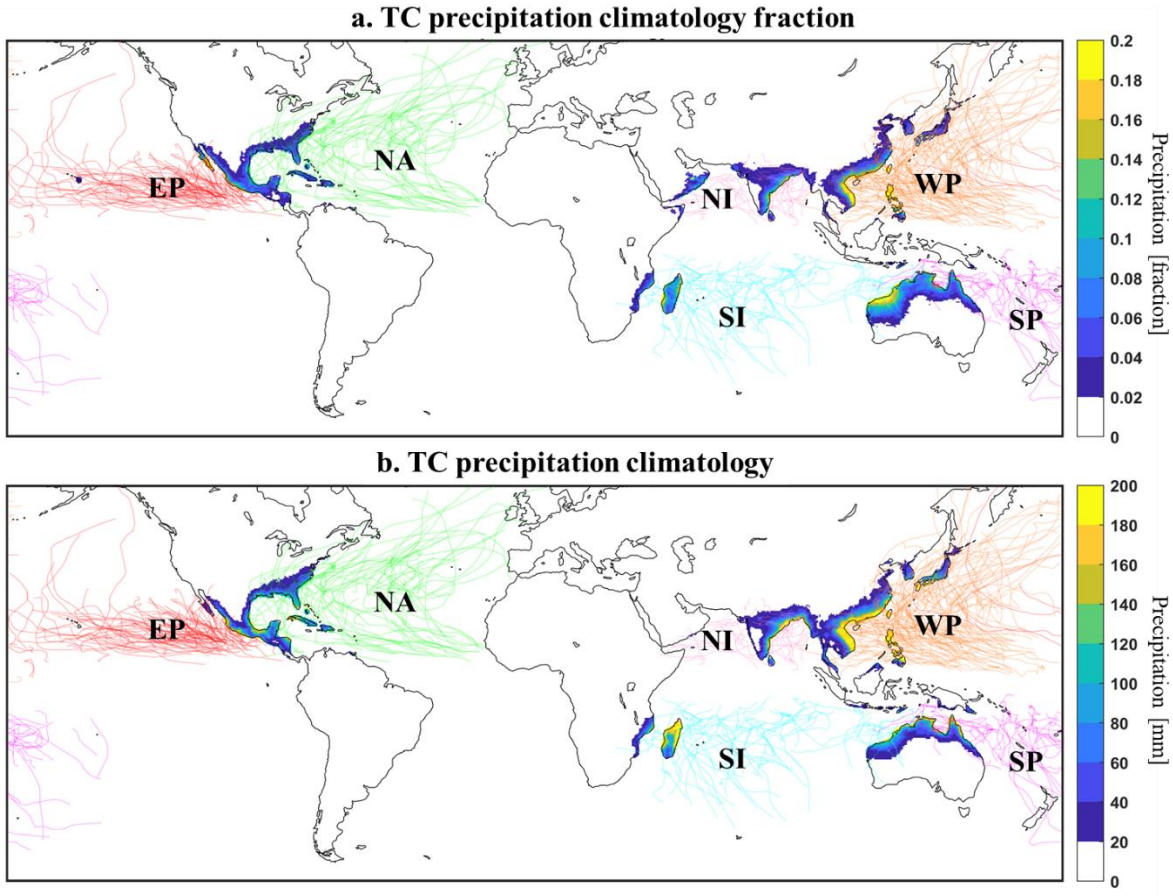

Figure 4-11. The distribution of landfalling TC precipitation over 1980-2019. a. TC precipitation climatology as a fraction of total precipitation climatology with color-coded lines indicating TC tracks over the 2015-2019 period. b. TC precipitation climatology in mm.

The variation in trends of TC precipitation is significant: one cannot extrapolate changes in activity in one basin and apply it to another, even for basins close in proximity (example: SI and SP). In order to give an overview of what changes in TC activity have occurred within each basin, we use the following criteria to grade changes of the $\langle R \rangle$, R_{90}, and R_{99}, $\langle V \rangle$, and $\sum V_{land}$ variables in Table 4.5:

- Little to no changes: >50% of the category is not seeing a significant change.
- Mixed changes: ≥50% of the category is seeing a significant change, but the trends are mixed between increasing and decreasing.
- Significantly increased: ≥50% and <100% of the category is seeing a significant positive change.

- Very significantly increased: 100% of the category has seen a significant positive change.

Percentages are calculated based on the number of intensity categories out of four (All, Weak, Strong, and Very Strong) that are seeing a significant trend for each variable. Though not independent of the other categories, the All TCs classification is included in the grading to ensure the Strong and Very Strong categories are not overrepresented against Weak TCs, which are the most frequent TC grade. In most cases, its inclusion does not change results. Note that the $\langle hV \rangle$ and $\langle hV_{land} \rangle$ variables are not considered, as they are closely related to TC precipitation rates.

Table 4-5. Summary of TC precipitation trends relating to precipitation rate percentile and volume totals across basins and at the global scale. Red text shows trends where at least 2 of 4 intensity classifications have experienced statistically significant positive changes in precipitation and bolded red text indicates categories with positive changes in precipitation in all intensity classifications.

	$\langle R \rangle$	R_{90}	R_{99}	$\langle V \rangle$	ΣV_{land}
EP	**Very significantly increased**	**Very significantly increased**	**Very significantly increased**	Little to no changes	Significantly increased
NA	Significantly increased	Significantly increased	Significantly increased	Significantly increased	Significantly increased
NI	Significantly increased	Significantly increased	**Very significantly increased**	Little to no changes	**Very significantly increased**
SI	**Very significantly increased**	**Very significantly increased**	**Very significantly increased**	Significantly increased	Little to no changes
SP	Significantly increased	Significantly increased	Significantly increased	Significantly increased	Significantly increased
WP	**Very significantly increased**	**Very significantly increased**	**Very significantly increased**	Mixed changes	Mixed changes
Global	**Very significantly increased**	**Very significantly increased**	**Very significantly increased**	Mixed changes	Significantly increased

4.4. Discussion

In this study, precipitation volumes and rates from TCs were investigated globally using robust regression tools, where it was shown that pronounced increases in TC precipitation rates can be observed across intensity categories and TC basins. These increases in precipitation rates have created increases in precipitation volumes over many basins and intensity categories, though global results are mixed. In terms of human impacts, greater precipitation totals over land were seen in all basins across categories, many influenced by global increases in TC precipitation along with changes in TC duration or landfalling frequency. Spatially, the most pronounced increases are occurring in North America and the Indian subcontinent. All basins are experiencing intensifying rainfall from TCs in one form or another, indicating changes in the Earth's hydroclimate over the 1980-2019 period. We hypothesize that observed changes are a result of increases in atmospheric water vapor following Clausius–

Clapeyron scaling, with possible contributions by anthropogenic aerosols (Zhao et al. 2018). However, results from Traxl et al. (2021) caution against using solely thermodynamical results to link detected changes to anthropogenic warming.

Global assessment of TC precipitation trends has been limited due to a lack of appropriate data. Concretely, the 2021 IPCC Working Group 1 summary (IPCC 2021; Section 8.3.2.5) reports a "low confidence" that there has been an increase in global TC precipitation, citing limitations in historical observations. Though not without uncertainty, the HRPCDRs methodology explored in this study translates historic satellite observations into data with global (land and water) coverage, a long and homogeneous temporal extent, and high-spatiotemporal resolution. This contrasts with studies that rely on gauge or radar-gauge data (Chang et al. 2013; Dhakal and Tharu 2018; Kunkel et al. 2010) that are the highest-quality measurements readily available for precipitation-oriented research but are limited by a lack of coverage over the oceans and in sparsely populated regions. Likewise, many studies that rely on satellite measurements are too limited in duration to overcome decade-scale climate oscillations that affect TC activity (Guzman and Jiang 2021; Skok et al. 2013). Moreover, high-resolution precipitation data sets like TMPA-3B42 (pre-version 7) and IMERG are also not developed to be homogeneous in extended time ranges. Current homogeneous satellite-based CDRs and reanalysis products available for long durations like PERSIANN-CDR or CHIRPS are available at spatiotemporal resolutions too coarse to resolve the topographically complex patterns of the TC cloud shield and movement of the mesoscale phenomenon. At the same time, this study is limited by using a static shape and size threshold to truncate TCs and by its reliance on a new and largely untested dataset that is still coarser in temporal resolution than the scale of TC dynamics.

Recently, a comparable study by Guzman & Jiang (2021) that was conducted using similar methods to this study and TMPA rainfall data uncovered an increasing trend of 1.3% a year in mean TC

precipitation rates and attributed it to increases in global mean temperature. This is significantly higher than the results from Figure 4.5, where global TC precipitation rates are shown to be increasing at a rate of 0.32±0.04% a year. Guzman & Jiang's results suggests a 21% increase in precipitation rates have occurred between 1998-2016. Using global mean SST data from NOAA NCEI's Climate at a Glance data portal (https://ww.ncdc.noaa.gov/cag/), an increase in global ocean SST of 0.28°C was recorded (note that Guzman & Jiang record this temperature as 0.21°C using SST measurements localized to TC tracks— Knutson et al. (2020) reports that tropical SST warms at a rate ~75% of global SST, so these numbers are consistent with each other). Guzman & Jiang's rate of 75%/°C is considerably higher than modeling studies' suggestion that an increase of 7% to ~14% (super Clausius-Clapeyron scaling) should occur per 1°C of global SST warming (Knutson et al. 2020). Over the same period (1998-2016), our methodology estimates a 2.1±1.3% (7.6%/°C) increase in precipitation rates (Figure 4.12), more in line with modeling projections than the quantities given in the comparative study. Our study suggests that over the last thirty years, an increase of 5.0±1.4% occurred during a warming of 0.45°C (11.1%/°C), again closer in line with modeling studies. The differences between studies are evident when considering mean precipitation values from each study over this period: the range of recorded yearly average precipitation rates from 1998-2016 measured by PDIR-CDR was 2.45–2.55 mm/hr, much larger and in a much smaller range than those recorded by TMPA-3B42 v7 using the 500 km truncation method (~1.7–2.4 mm/hr). Over the entire 40-year period, precipitation averages recorded by PDIR-CDR range from 1.82–2.55 mm/hr. Clearly, the choice of precipitation data set plays a very significant role in the results recorded between studies.

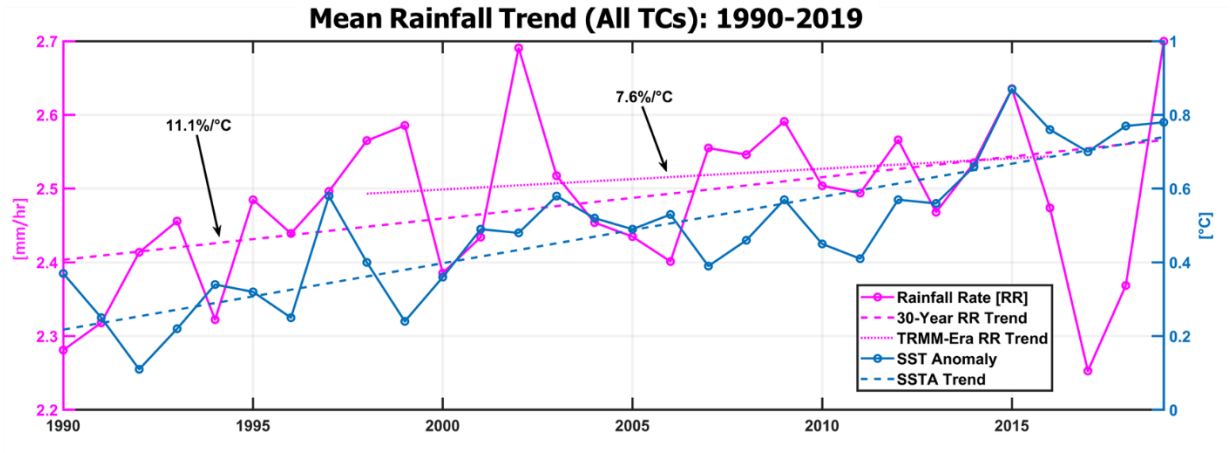

Figure 4-12. Mean precipitation rate values from All TCs (no smoothing) measured by PDIR-CDR during the 1990-2019 period (magenta) compared to sea surface temperature anomaly measurements (blue) from NOAA NCEI's Climate at a Glance data portal. Two trends are analyzed: 30-year (1990-2019) and TRMM-era (1998-2016), which show an increase in precipitation rates of 11.1%/C and 7.6%/C, respectively.

Continued improvement of HRPCDRs like PDIR-CDR and the passage of time will shed further light on how precipitation in historic TCs has evolved because of anthropogenic influence. At this time, further analysis into how climate oscillations influence the variability in TC precipitation properties, identifying when anthropogenic warming began to affect TC characteristics in longer duration historic data sets, and merging observed historical trends with projected future trends are vital to further understanding the past, present, and future of TC precipitation. As TC-linked disasters are becoming more commonplace, our continued understanding of their nature is vital to ensure global security of our coastlines, population centers, and vital infrastructure.

Chapter 5 - Summary and Conclusions

5.1. Dissertation Summary and Conclusions

The emergence of HRPCDRs has made retrospective analysis of climate change signals in the hydroclimate more detectable with greater accuracy and longer evaluation periods than have been possible in the past. Paired with innovative data mining tools and robust statistical analysis, ARs and TCs were studied over time periods long enough to uncover trends with uncertainty levels sufficiently reduced as to overcome the influence of decades-scale climate oscillations that add significant noise to the system. These two topics were the subjects of two publication-style scientific reports produced by the dissertation author, of which one was published (Shearer et al. 2020) while the other currently sits in production (Shearer et al. 2022). Concretely, the first article (Chapter 3) overviews the creation of an object-oriented AR tracking method that was developed to study the evolution of ARs and their precipitation. Results from this study showed robust intensification signals in the intensity, duration, and size of ARs over the 1983-2016 study period, all linked to increases in the concentration of atmospheric water vapor robustly observed over the period. In the second study (Chapter 4), the dissertation author worked closely with the developer of the PDIR algorithm to produce a high-fidelity and spatiotemporally homogeneous data record of precipitation spanning 40 years and corrected at the monthly scale by a gauge-derived product. This dataset, named PDIR-CDR, was used to measure the evolution of TC precipitation globally and across basins during the study period of 1980-2019. This study found that precipitation rates have occurred globally and over every basin studied. Furthermore, TC precipitation volumes and their contributions to yearly precipitation totals over population centers have intensified in many basins, which have also produced a global signal. It was shown that these increases in precipitation are likely linked to anthropogenic warming, as the rate they have increased matches expectations outlined by the Clausius-Clapeyron relationship.

At a high level, the main contributions of this dissertation to the scientific domain are as follows:

- **Developed the first global AR tracking methodology that uses an IVT threshold tied to precipitation. This AR tracking methodology was able to capture the climatological signature of AR tracks uncovered by other methodologies without using geometric constraints; instead, it was found that tracking ARs by their higher intensity cores and using region growing segmentation to assign AR bodies to cores was a sufficient mechanism to extract AR lifecycles, with a 99.99% success rate.**
- **Found that the global frequency of AR lifecycles over the 1983-2016 period was cyclical in nature, while the time-series of precipitation, duration, and size show robust increasing signatures. Specifically, from 1992 to 2016, AR contributions to global precipitation climatology rose from 17% to 21%.**
- **Discovered that the frequency of ARs between the Northern and Southern hemisphere followed the proportion of AR hot spots (2:3) discovered in Sellars et al. (2017) and other studies suggesting symmetry in AR formation rates.**
- **Proved the newly developed PDIR-CDR's temporal homogeneity in the tropics and its utility as a high-resolution climate data record of precipitation.**
- **Uncovered a 40-year global signal of intensifying precipitation from tropical cyclones, the longest duration study done for global tropical cyclone rainfall yet.**
- **Though not the first study to identify historic increases in tropical cyclone precipitation rates and not the first to attribute it to anthropogenic warming, this is the first study to detect observed increases in tropical cyclone precipitation consistent with expectations following the Clausius-Clapeyron relationship.**

- **Determined that every major tropical cyclone basin has seen precipitation intensification by multiple examined metrics.**
- **Found evidence that precipitation from both global ARs and TCs has been influenced by anthropogenic climate change.**

5.2. Future Directions

5.2.1. High Resolution Precipitation Climate Data Records

HRPCDRs are a new tool in a field seeing rapid advancement as new cutting-edge techniques are developed to overcome the inherent uncertainty of satellite remotely sensed precipitation. Continued improvements in the temporal homogeneity and accuracy of HRPCDRs will serve to increase the accuracy of detected trends. For instance, adapting additional reanalysis datasets into the input of PDIR-CDR and other HRPCDRs could help fill gaps in the satellite record and help improve precipitation measurements over the upper latitudes, where reanalysis datasets tend to overperform satellite products. Likewise, bias correction with gauges using quantile mapping or other techniques can improve data accuracy over land.

Moreover, the passage of time will allow our retrospective analysis of trends in hydroclimate extremes to be extended to longer durations. As our satellite records moves into the half-a-century realm this decade, we may better pinpoint where the anthropogenic warming has affected our hydroclimate.

5.2.2. Atmospheric River Tracking

Though AR-CONNECT significantly improves upon the original CONNECT design for tracking ARs, there are several improvements that could feasibly improve AR segmentation and increase its utility. First, though AR-CONNECT largely solves the conglomerate object problem defined in Chapter 3, there still exist a very small (<1% of the catalog) but non-inconsequential number of conglomerate objects that perhaps skew results. In theory, a single conglomerate object can contain

many individual AR lifecycles and negating one conglomerate object from our analyses can lead to underestimation in the frequency of ARs, along with other AR-related variables (the exact impact that negating conglomerate objects has on the results is at this time unknown.) Using a variable threshold technique like that described in Skok et al. (2013) that applies several segmentation levels could better separate AR lifecycles and therefore improve results. However, attempts to implement such a technique in the project overviewed in Chapter 3 were limited by large RAM requirements that available computational resources could not accommodate.

The results of Collow et al. (2022), of which AR-CONNECT is a participating algorithm, show that there is considerable variance in the results of any AR detection technique depending on what reanalysis data set is chosen to be used as forcing data. The aforementioned study recommends that future studies with AR detection techniques should consider using multiple reanalyses to test hypotheses to limit data bias from creating artificial results. Therefore, future analysis of precipitation using AR-CONNECT would benefit from this approach, where these products could limit uncertainty in the segmentation of AR lifecycles. Given that the trend results presented in Chapter 3 largely match those presented in Collow et al. (2022), it was determined that re-evaluating Chapter 3's results using multiple reanalyses was not necessary at this time.

The following project ideas are outside the precipitation-oriented scope of this dissertation but would likely be of considerable interest to an investigator focused on the atmospheric dynamics of ARs. They are included for the sake of thoroughness:

The IVT threshold used in AR-CONNECT is tied to AR impacts in the mid-latitudes, especially for regions with considerable orographic lift (Rutz et al. 2014). However, during the course of the "Application of Remote Sensing Precipitation Data and the CONNECT algorithm to Investigate Spatiotemporal Variations of Heavy Precipitation: Case Study of Major Floods Across Iran (Spring

2019)" study, it was seen that AR-CONNECT's ability to detect ARs in regions outside of the coastal mid-latitudes like Iran (Sadeghi et al. 2021a), Antarctica (Wille et al. 2019), among others (this limitation as discovered during the In order to produce a truly global AR tracking methodology—at the expense of no longer having a method tied to impacts—IVT thresholds used by AR-CONNECT could be adapted to a climatological- or latitude-based threshold like tARget or Lavers and Villarini, respectively. Concretely, we hypothesize that the seeded region-growing segmentation method used in AR-CONNECT could be adapted to fill in AR bodies at the 85th percentile of IVT using seeds segmented from the 95th+ percentile of IVT.

Moreover, positive changes in water vapor concentrations in the atmosphere have emerged from a warming climate. As such, the climatology of global IVT has increased, meaning IVT values above low-level thresholds are becoming more commonplace. From a dynamics point of view (as opposed to impacts), this means detection techniques using static thresholds are detecting ARs more frequently than in the past. This can be seen by the robust increasing signal in AR size shown in Figure 3.6. For research concerned with AR dynamics, it may be worth considering a temporally varying IVT threshold that changes according to how the IVT field evolves, so that detected ARs are similarly anomalous events throughout the study period.

5.2.3. Tropical Cyclone Segmentation

Though the 500 km radius threshold used in Chapter 4 is a common technique in AR literature for segmentation, it is well-established that such a rigid structure can overestimate (underestimate) precipitation totals from small (large) TCs. Using a better metric to classify TC size like outmost closed isobar would serve to improve TC segmentation and therefore improve calculations of annual TC volume, overland precipitation totals, and precipitation rates. At this time, no publicly available method to determined outermost closed isobar exists (for more information, see Section 4.2.2).

References

Adams, R., and L. Bischof, 1994: Seeded Region Growing. *IEEE Transactions on Pattern Analysis and Machine Intelligence*, **16**, 641–647, https://doi.org/10.1109/34.295913.

Adler, R. F., and Coauthors, 2018: The Global Precipitation Climatology Project (GPCP) Monthly Analysis (New Version 2.3) and a Review of 2017 Global Precipitation. *Atmosphere 2018, Vol. 9, Page 138*, **9**, 138, https://doi.org/10.3390/ATMOS9040138.

AghaKouchak, A., N. Nasrollahi, J. Li, B. Imam, and S. Sorooshian, 2011: Geometrical characterization of precipitation patterns. *Journal of Hydrometeorology*, **12**, 274–285, https://doi.org/10.1175/2010JHM1298.1.

Akbari Asanjan, A., T. Yang, K. Hsu, S. Sorooshian, J. Lin, and Q. Peng, 2018: Short-Term Precipitation Forecast Based on the PERSIANN System and LSTM Recurrent Neural Networks. *Journal of Geophysical Research: Atmospheres*, **123**, 12,543-12,563, https://doi.org/10.1029/2018JD028375.

Ashouri, H., K. L. Hsu, S. Sorooshian, D. K. Braithwaite, K. R. Knapp, L. D. Cecil, B. R. Nelson, and O. P. Prat, 2015: PERSIANN-CDR: Daily Precipitation Climate Data Record from Multisatellite Observations for Hydrological and Climate Studies. *Bull Am Meteorol Soc*, **96**, 69–83, https://doi.org/10.1175/BAMS-D-13-00068.1.

Bakkensen, L. A., and R. O. Mendelsohn, 2019: Global Tropical Cyclone Damages and Fatalities Under Climate Change: An Updated Assessment. 179–197, https://doi.org/10.1007/978-3-030-02402-4_9.

Balaji, M., A. Chakraborty, and M. Mandal, 2018: Changes in tropical cyclone activity in north Indian Ocean during satellite era (1981–2014). *International Journal of Climatology*, **38**, 2819–2837, https://doi.org/10.1002/JOC.5463.

Brands, S., J. M. Gutiérrez, and D. San-Martín, 2017: Twentieth-century atmospheric river activity along the west coasts of Europe and North America: algorithm formulation, reanalysis uncertainty and links to atmospheric circulation patterns. *Climate Dynamics*, **48**, 2771–2795, https://doi.org/10.1007/S00382-016-3095-6.

Chang, C. P., Y. T. Yang, and H. C. Kuo, 2013: Large Increasing Trend of Tropical Cyclone Rainfall in Taiwan and the Roles of Terrain. *Journal of Climate*, **26**, 4138–4147, https://doi.org/10.1175/JCLI-D-12-00463.1.

Changnon, S. A., and K. E. Kunkel, 1995: Climate-Related Fluctuations in Midwestern Floods during 19211985. *Journal of Water Resources Planning and Management*, **121**, 326–334, https://doi.org/10.1061/(ASCE)0733-9496(1995)121:4(326).

Chavas, D. R., and K. A. Emanuel, 2010: A QuikSCAT climatology of tropical cyclone size. *Geophysical Research Letters*, **37**, 18816, https://doi.org/10.1029/2010GL044558.

Chen, L., and L. Wang, 2018: Recent advance in earth observation big data for hydrology. *https://doi.org/10.1080/20964471.2018.1435072*, **2**, 86–107, https://doi.org/10.1080/20964471.2018.1435072.

Collow, A. B. M., and Coauthors, 2022: An Overview of ARTMIP's Tier 2 Reanalysis Intercomparison: Uncertainty in the Detection of Atmospheric Rivers and Their Associated Precipitation. *Journal of Geophysical Research: Atmospheres*, **127**, https://doi.org/10.1029/2021JD036155.

Daly, C., 2006: Guidelines for assessing the suitability of spatial climate data sets. *International Journal of Climatology*, **26**, 707–721, https://doi.org/10.1002/JOC.1322.

Dettinger, M. D., 2011: Climate change, atmospheric rivers, and floods in California - a multimodel analysis of storm frequency and magnitude changes. *J Am Water Resour Assoc*, https://doi.org/10.1111/j.1752-1688.2011.00546.x.

——, M., 2013: Atmospheric rivers as drought busters on the U.S. West Coast. *Journal of Hydrometeorology*, **14**, 1721–1732, https://doi.org/10.1175/JHM-D-13-02.1.

Dezfuli, A., 2020: Rare atmospheric river caused record floods across the middle east. *Bull Am Meteorol Soc*, **101**, E394–E400, https://doi.org/10.1175/BAMS-D-19-0247.1.

Dhakal, N., and B. Tharu, 2018: Spatio-temporal trends in daily precipitation extremes and their connection with North Atlantic tropical cyclones for the southeastern United States. *International Journal of Climatology*, **38**, 3822–3831, https://doi.org/10.1002/JOC.5535.

Domingues, R., and Coauthors, 2021: Ocean Conditions and the Intensification of Three Major Atlantic Hurricanes in 2017. *Monthly Weather Review*, **149**, 1265–1286, https://doi.org/10.1175/MWR-D-20-0100.1.

Dube, S. K., I. Jain, A. D. Rao, and T. S. Murty, 2009: Storm surge modelling for the Bay of Bengal and Arabian Sea. *Natural Hazards*, **51**, 3–27, https://doi.org/10.1007/S11069-009-9397-9/FIGURES/15.

Dumouchel, W., 1992: Integrating a Robust Option into a Multiple Regression Computing Environment. https://doi.org/10.1007/978-1-4613-9154-8_3.

Easterling, D. R., J. Arnold, T. Knutson, K. Kunkel, A. LeGrande, and L. Ruby, 2017: DigitalCommons@University of Nebraska-Lincoln Precipitation change in the United States.

Esfandiari, N., and H. Lashkari, 2021: The effect of atmospheric rivers on cold-season heavy precipitation events in Iran. *Journal of Water and Climate Change*, **12**, 596–611, https://doi.org/10.2166/WCC.2020.259.

Espinoza, V., D. E. Waliser, B. Guan, D. A. Lavers, and F. M. Ralph, 2018: Global Analysis of Climate Change Projection Effects on Atmospheric Rivers. *Geophysical Research Letters*, **45**, 4299–4308, https://doi.org/10.1029/2017GL076968.

Feldmann, M., K. Emanuel, L. Zhu, and U. Lohmann, 2019: Estimation of Atlantic Tropical Cyclone Rainfall Frequency in the United States. *Journal of Applied Meteorology and Climatology*, **58**, 1853–1866, https://doi.org/10.1175/JAMC-D-19-0011.1.

Fowler, H. J., and Coauthors, 2021: Anthropogenic intensification of short-duration rainfall extremes. *Nature Reviews Earth & Environment 2021 2:2*, **2**, 107–122, https://doi.org/10.1038/s43017-020-00128-6.

Gao, S., J. Mao, W. Zhang, F. Zhang, and X. Shen, 2021: Atmospheric moisture shapes increasing tropical cyclone precipitation in southern China over the past four decades. *Environmental Research Letters*, **16**, 34004, https://doi.org/10.1088/1748-9326/ABD78A.

Gelaro, R., and Coauthors, 2017: The modern-era retrospective analysis for research and applications, version 2 (MERRA-2). *Journal of Climate*, **30**, 5419–5454, https://doi.org/10.1175/JCLI-D-16-0758.1.

Gorodetskaya, I. v., M. Tsukernik, K. Claes, M. F. Ralph, W. D. Neff, and N. P. M. van Lipzig, 2014: The role of atmospheric rivers in anomalous snow accumulation in East Antarctica. *Geophysical Research Letters*, **41**, 6199–6206, https://doi.org/10.1002/2014GL060881.

Gorooh, V. A., S. Kalia, P. Nguyen, K. lin Hsu, S. Sorooshian, S. Ganguly, and R. R. Nemani, 2020: Deep Neural Network Cloud-Type Classification (DeepCTC) Model and Its Application in Evaluating PERSIANN-CCS. *Remote Sensing 2020, Vol. 12, Page 316*, **12**, 316, https://doi.org/10.3390/RS12020316.

Greve, P., B. Orlowsky, B. Mueller, J. Sheffield, M. Reichstein, and S. I. Seneviratne, 2014: Global assessment of trends in wetting and drying over land. *Nature Geoscience 2014 7:10*, **7**, 716–721, https://doi.org/10.1038/ngeo2247.

Guan, B., and D. E. Waliser, 2015: Detection of atmospheric rivers: Evaluation and application of an algorithm for global studies. *Journal of Geophysical Research*, **120**, 12,514-12,535, https://doi.org/10.1002/2015JD024257.

——, and ——, 2019: Tracking Atmospheric Rivers Globally: Spatial Distributions and Temporal Evolution of Life Cycle Characteristics. *Journal of Geophysical Research: Atmospheres*, **124**, 12523–12552, https://doi.org/10.1029/2019JD031205.

——, N. P. Molotch, D. E. Waliser, E. J. Fetzer, and P. J. Neiman, 2010: Extreme snowfall events linked to atmospheric rivers and surface air temperature via satellite measurements. *Geophysical Research Letters*, **37**, https://doi.org/10.1029/2010GL044696.

Guo, H., A. Bao, T. Liu, S. Chen, and F. Ndayisaba, 2016: Evaluation of PERSIANN-CDR for meteorological drought monitoring over China. *Remote Sensing*, **8**, https://doi.org/10.3390/RS8050379.

Guzman, O., and H. Jiang, 2021: Global increase in tropical cyclone rain rate. *Nature Communications 2021 12:1*, **12**, 1–8, https://doi.org/10.1038/s41467-021-25685-2.

Hampel, F. R., 1986: Robust statistics : the approach based on influence functions. 502.

Hayatbini, N., and Coauthors, 2019: Conditional Generative Adversarial Networks (cGANs) for Near Real-Time Precipitation Estimation from Multispectral GOES-16 Satellite Imageries—PERSIANN-cGAN. *Remote Sensing 2019, Vol. 11, Page 2193*, **11**, 2193, https://doi.org/10.3390/RS11192193.

Hey, T., S. Tansley, and K. Tolle, 2009: The Fourth Paradigm: Data-Intensive Scientific Discovery.

Hong, Y., K. L. Hsu, S. Sorooshian, and X. Gao, 2004: Precipitation Estimation from Remotely Sensed Imagery Using an Artificial Neural Network Cloud Classification System. *Journal of Applied Meteorology and Climatology*, **43**, 1834–1853, https://doi.org/10.1175/JAM2173.1.

Hsu, K. L., X. Gao, S. Sorooshian, and H. v. Gupta, 1997: Precipitation estimation from remotely sensed information using artificial neural networks. *Journal of Applied Meteorology*, https://doi.org/10.1175/1520-0450(1997)036<1176:PEFRSI>2.0.CO;2.

Huang, W.-R., P.-Y. Liu, and J. Hsu, 2021: Multiple timescale assessment of wet season precipitation estimation over Taiwan using the PERSIANN family products. *International Journal of Applied Earth Observation and Geoinformation*, **103**, 102521, https://doi.org/10.1016/J.JAG.2021.102521.

IPCC, 2012: Managing the Risks of Extreme Events and Disasters to Advance Climate Change Adaptation — IPCC.

——, 2021: Sixth Assessment Report: Working Group 1.

Jackson, D. L., M. Hughes, and G. A. Wick, 2016: Evaluation of landfalling atmospheric rivers along the U.S. West Coast in reanalysis data sets. *Journal of Geophysical Research*, **121**, 2705–2718, https://doi.org/10.1002/2015JD024412.

Jiang, H., and E. J. Zipser, 2010: Contribution of Tropical Cyclones to the Global Precipitation from Eight Seasons of TRMM Data: Regional, Seasonal, and Interannual Variations. *Journal of Climate*, **23**, 1526–1543, https://doi.org/10.1175/2009JCLI3303.1.

Kelley, O. A., 2014: Where the least rainfall occurs in the sahara desert, the TRMM radar reveals a different pattern of rainfall each season. *Journal of Climate*, **27**, 6919–6939, https://doi.org/10.1175/JCLI-D-14-00145.1.

Knapp, K. R., M. C. Kruk, D. H. Levinson, H. J. Diamond, and C. J. Neumann, 2010: The International Best Track Archive for Climate Stewardship (IBTrACS): Unifying Tropical Cyclone Data. *Bull Am Meteorol Soc*, **91**, 363–376, https://doi.org/10.1175/2009BAMS2755.1.

Knutson, T., and Coauthors, 2020: Tropical Cyclones and Climate Change Assessment: Part II: Projected Response to Anthropogenic Warming. *Bull Am Meteorol Soc*, **101**, E303–E322, https://doi.org/10.1175/BAMS-D-18-0194.1.

——, and Coauthors, 2010: Tropical cyclones and climate change. *Nature Geoscience 2010 3:3*, **3**, 157–163, https://doi.org/10.1038/ngeo779.

Kossin, J. P., 2018: A global slowdown of tropical-cyclone translation speed. *Nature 2018 558:7708*, **558**, 104–107, https://doi.org/10.1038/s41586-018-0158-3.

Kunkel, K. E., and Coauthors, 2010: Recent increases in U.S. heavy precipitation associated with tropical cyclones. *Geophysical Research Letters*, **37**, https://doi.org/10.1029/2010GL045164.

Landsea, C. W., G. A. Vecchi, L. Bengtsson, and T. R. Knutson, 2010: Impact of Duration Thresholds on Atlantic Tropical Cyclone Counts. *Journal of Climate*, **23**, 2508–2519, https://doi.org/10.1175/2009JCLI3034.1.

Larson, J., Y. Zhou, and R. W. Higgins, 2005: Characteristics of Landfalling Tropical Cyclones in the United States and Mexico: Climatology and Interannual Variability. *Journal of Climate*, **18**, 1247–1262, https://doi.org/10.1175/JCLI3317.1.

Lau, K. M., Y. P. Zhou, and H. T. Wu, 2008: Have tropical cyclones been feeding more extreme rainfall? *Journal of Geophysical Research: Atmospheres*, **113**, 23113, https://doi.org/10.1029/2008JD009963.

Lavender, S. L., and J. L. McBride, 2021: Global climatology of rainfall rates and lifetime accumulated rainfall in tropical cyclones: Influence of cyclone basin, cyclone intensity and cyclone size. *International Journal of Climatology*, **41**, E1217–E1235, https://doi.org/10.1002/JOC.6763.

Lavers, D. A., and G. Villarini, 2015: The contribution of atmospheric rivers to precipitation in Europe and the United States. *JOURNAL OF HYDROLOGY*, **522**, 382–390, https://doi.org/10.1016/j.jhydrol.2014.12.010.

Li, L., and P. Chakraborty, 2020: Slower decay of landfalling hurricanes in a warming world. *Nature 2020 587:7833*, **587**, 230–234, https://doi.org/10.1038/s41586-020-2867-7.

Lin, Y., M. Zhao, and M. Zhang, 2015: Tropical cyclone rainfall area controlled by relative sea surface temperature. *Nature Communications*, **6**, https://doi.org/10.1038/NCOMMS7591.

Liu, L., and Y. Wang, 2020: Trends in Landfalling Tropical Cyclone–Induced Precipitation over China. *Journal of Climate*, **33**, 2223–2235, https://doi.org/10.1175/JCLI-D-19-0693.1.

Martin Ralph, F., J. J. Rutz, J. M. Cordeira, M. Dettinger, M. Anderson, D. Reynolds, L. J. Schick, and C. Smallcomb, 2019: A scale to characterize the strength and impacts of atmospheric rivers. *Bull Am Meteorol Soc*, **100**, 269–289, https://doi.org/10.1175/BAMS-D-18-0023.1.

Maxwell, J. T., J. C. Bregy, S. M. Robeson, P. A. Knapp, P. T. Soulé, and V. Trouet, 2021: Recent increases in tropical cyclone precipitation extremes over the US east coast. *Proc Natl Acad Sci U S A*, **118**, https://doi.org/10.1073/PNAS.2105636118/-/DCSUPPLEMENTAL.

Mendelsohn, R., K. Emanuel, S. Chonabayashi, and L. Bakkensen, 2012: The impact of climate change on global tropical cyclone damage. 15, https://doi.org/10.1038/NCLIMATE1357.

Miao, C., H. Ashouri, K. L. Hsu, S. Sorooshian, and Q. Duan, 2015: Evaluation of the PERSIANN-CDR daily rainfall estimates in capturing the behavior of extreme precipitation events over China. *Journal of Hydrometeorology*, **16**, 1387–1396, https://doi.org/10.1175/JHM-D-14-0174.1.

Montini, T. L., C. Jones, and L. M. V. Carvalho, 2019: The South American Low-Level Jet: A New Climatology, Variability, and Changes. *Journal of Geophysical Research: Atmospheres*, **124**, 1200–1218, https://doi.org/10.1029/2018JD029634.

Mundhenk, B. D., E. A. Barnes, and E. D. Maloney, 2016: All-season climatology and variability of atmospheric river frequencies over the North Pacific. *Journal of Climate*, **29**, 4885–4903, https://doi.org/10.1175/JCLI-D-15-0655.1.

Musser, J. W., K. M. Watson, and A. J. Gotvald, 2017: Characterization of peak streamflows and flood inundation at selected areas in North Carolina following Hurricane Matthew, October 2016. *Open-File Report*, https://doi.org/10.3133/OFR20171047.

Neiman, P. J., M. F. Ralph, B. J. Moore, M. Hughes, K. M. Mahoney, J. M. Cordeira, and M. D. Dettinger, 2013: The landfall and inland penetration of a flood-producing atmospheric river in Arizona. Part I: Observed synoptic-scale, orographic, and hydrometeorological characteristics. *Journal of Hydrometeorology*, **14**, 460–484, https://doi.org/10.1175/JHM-D-12-0101.1.

Nguyen, P., S. Sellars, A. Thorstensen, Y. Tao, H. Ashouri, D. Braithwaite, K. Hsu, and S. Sorooshian, 2014: Satellites Track Precipitation of Super Typhoon Haiyan. *Eos, Transactions American Geophysical Union*, **95**, 133–135, https://doi.org/10.1002/2014EO160002.

——, M. Ombadi, S. Sorooshian, K. Hsu, A. AghaKouchak, D. Braithwaite, H. Ashouri, and A. Rose Thorstensen, 2018a: The PERSIANN family of global satellite precipitation data: A review and evaluation of products. *Hydrology and Earth System Sciences*, **22**, 5801–5816, https://doi.org/10.5194/HESS-22-5801-2018.

——, A. Thorstensen, S. Sorooshian, K. Hsu, A. AghaKouchak, H. Ashouri, H. Tran, and D. Braithwaite, 2018b: Global Precipitation Trends across Spatial Scales Using Satellite Observations. *Bull Am Meteorol Soc*, **99**, 689–697, https://doi.org/10.1175/BAMS-D-17-0065.1.

——, and Coauthors, 2019: The CHRS data portal, an easily accessible public repository for PERSIANN global satellite precipitation data. *Scientific Data*, **6**, https://doi.org/10.1038/SDATA.2018.296.

——, and Coauthors, 2020a: PERSIANN Dynamic Infrared–Rain Rate (PDIR-Now): A Near-Real-Time, Quasi-Global Satellite Precipitation Dataset. *Journal of Hydrometeorology*, **21**, 2893–2906, https://doi.org/10.1175/JHM-D-20-0177.1.

——, E. J. Shearer, M. Ombadi, V. A. Gorooh, K. Hsu, S. Sorooshian, W. S. Logan, and M. Ralph, 2020b: PERSIANN Dynamic Infrared–Rain Rate Model (PDIR) for High-Resolution, Real-Time Satellite Precipitation Estimation. *Bull Am Meteorol Soc*, **101**, E286–E302, https://doi.org/10.1175/BAMS-D-19-0118.1.10.1175/BAMS-D-19-0118.1.

O'Brien, T. A., and Coauthors, 2022: Increases in Future AR Count and Size: Overview of the ARTMIP Tier 2 CMIP5/6 Experiment. *Journal of Geophysical Research: Atmospheres*, **127**, https://doi.org/10.1029/2021JD036013.

van Oldenborgh, G. J., and Coauthors, 2017: Attribution of extreme rainfall from Hurricane Harvey, August 2017. *Environmental Research Letters*, **12**, 124009, https://doi.org/10.1088/1748-9326/AA9EF2.

Ombadi, M., P. Nguyen, S. Sorooshian, and K. lin Hsu, 2018: Developing Intensity-Duration-Frequency (IDF) Curves From Satellite-Based Precipitation: Methodology and Evaluation. *Water Resources Research*, https://doi.org/10.1029/2018WR022929.

Omranian, E., H. O. Sharif, and A. A. Tavakoly, 2018: How Well Can Global Precipitation Measurement (GPM) Capture Hurricanes? Case Study: Hurricane Harvey. *Remote Sensing 2018, Vol. 10, Page 1150*, **10**, 1150, https://doi.org/10.3390/RS10071150.

Paerl, H. W., N. S. Hall, A. G. Hounshell, R. A. Luettich, K. L. Rossignol, C. L. Osburn, and J. Bales, 2019: Recent increase in catastrophic tropical cyclone flooding in coastal North Carolina, USA: Long-term observations suggest a regime shift. *Scientific Reports 2019 9:1*, **9**, 1–9, https://doi.org/10.1038/s41598-019-46928-9.

Pan, B., K. Hsu, A. AghaKouchak, and S. Sorooshian, 2019: Improving Precipitation Estimation Using Convolutional Neural Network. *Water Resources Research*, **55**, 2301–2321, https://doi.org/10.1029/2018WR024090.

Patricola, C. M., and M. F. Wehner, 2018: Anthropogenic influences on major tropical cyclone events. *Nature 2018 563:7731*, **563**, 339–346, https://doi.org/10.1038/s41586-018-0673-2.

Pavlidis, T., 1979: Filling algorithms for raster graphics. *Computer Graphics and Image Processing*, **10**, 126–141, https://doi.org/10.1016/0146-664X(79)90046-7.

Payne, A. E., and G. Magnusdottir, 2014: Dynamics of landfalling atmospheric rivers over the North Pacific in 30 years of MERRA reanalysis. *Journal of Climate*, **27**, 7133–7150, https://doi.org/10.1175/JCLI-D-14-00034.1.

Peterson, T. C., T. R. Karl, J. P. Kossin, K. E. Kunkel, J. H. Lawrimore, J. R. McMahon, R. S. Vose, and X. Yin, 2013: Changes in weather and climate extremes: State of knowledge relevant to air and water quality in the United States. *http://dx.doi.org/10.1080/10962247.2013.851044*, **64**, 184–197, https://doi.org/10.1080/10962247.2013.851044.

Prat, O. P., and B. R. Nelson, 2013: Precipitation Contribution of Tropical Cyclones in the Southeastern United States from 1998 to 2009 Using TRMM Satellite Data. *Journal of Climate*, **26**, 1047–1062, https://doi.org/10.1175/JCLI-D-11-00736.1.

Ralph, F. M., and M. D. Dettinger, 2011: Storms, floods, and the science of atmospheric rivers. *Eos (Washington DC)*, https://doi.org/10.1029/2011EO320001.

——, P. J. Neiman, and G. A. Wick, 2004: Satellite and CALJET aircraft observations of atmospheric rivers over the Eastern North Pacific Ocean during the winter of 1997/98. *Monthly Weather Review*, https://doi.org/10.1175/1520-0493(2004)132<1721:SACAOO>2.0.CO;2.

——, ——, ——, S. I. Gutman, M. D. Dettinger, D. R. Cayan, and A. B. White, 2006: Flooding on California's Russian River: Role of atmospheric rivers. *Geophysical Research Letters*, **33**, https://doi.org/10.1029/2006GL026689.

——, M. C. L. D. Dettinger, M. M. Cairns, T. J. Galarneau, and J. Eylander, 2018: Defining "Atmospheric River": How the Glossary of Meteorology Helped Resolve a Debate. *Bull Am Meteorol Soc*, **99**, 837–839, https://doi.org/10.1175/BAMS-D-17-0157.1.

Ramos, A. M., R. M. Trigo, M. L. R. Liberato, and R. Tomé, 2015: Daily precipitation extreme events in the Iberian Peninsula and its association with atmospheric rivers. *Journal of Hydrometeorology*, **16**, 579–597, https://doi.org/10.1175/JHM-D-14-0103.1.

——, M. J. Martins, R. Tomé, and R. M. Trigo, 2018: Extreme Precipitation Events in Summer in the Iberian Peninsula and Its Relationship With Atmospheric Rivers. *Frontiers in Earth Science*, **6**, https://doi.org/10.3389/FEART.2018.00110.

Rappaport, E. N., 2014: Fatalities in the United States from Atlantic Tropical Cyclones: New Data and Interpretation. *Bull Am Meteorol Soc*, **95**, 341–346, https://doi.org/10.1175/BAMS-D-12-00074.1.

Reed, K. A., A. M. Stansfield, M. F. Wehner, and C. M. Zarzycki, 2020: Forecasted attribution of the human influence on Hurricane Florence. *Science Advances*, **6**, https://doi.org/10.1126/SCIADV.AAW9253/SUPPL_FILE/AAW9253_SM.PDF.

Rhoades, A. M., A. D. Jones, T. A. O'Brien, J. P. O'Brien, P. A. Ullrich, and C. M. Zarzycki, 2020: Influences of North Pacific Ocean Domain Extent on the Western U.S. Winter Hydroclimatology in Variable-Resolution CESM. *Journal of Geophysical Research: Atmospheres*, **125**, https://doi.org/10.1029/2019JD031977.

Rienecker, M. M., and Coauthors, 2011: MERRA: NASA's modern-era retrospective analysis for research and applications. *Journal of Climate*, **24**, 3624–3648, https://doi.org/10.1175/JCLI-D-11-00015.1.

Risser, M. D., and M. F. Wehner, 2017: Attributable Human-Induced Changes in the Likelihood and Magnitude of the Observed Extreme Precipitation during Hurricane Harvey. *Geophysical Research Letters*, **44**, 12, 412–457, 464, https://doi.org/10.1002/2017GL075888.

Rutz, J. J., W. James Steenburgh, and F. Martin Ralph, 2014: Climatological characteristics of atmospheric rivers and their inland penetration over the western united states. *Monthly Weather Review*, **142**, 905–921, https://doi.org/10.1175/MWR-D-13-00168.1.

——, and Coauthors, 2019: The Atmospheric River Tracking Method Intercomparison Project (ARTMIP): Quantifying Uncertainties in Atmospheric River Climatology. *Journal of Geophysical Research: Atmospheres*, **124**, 13777–13802, https://doi.org/10.1029/2019JD030936.

Sadeghi, M., and Coauthors, 2021a: Application of remote sensing precipitation data and the CONNECT algorithm to investigate spatiotemporal variations of heavy precipitation: Case study of major floods across Iran (Spring 2019). *Journal of Hydrology*, **600**, https://doi.org/10.1016/J.JHYDROL.2021.126569.

——, P. Nguyen, M. R. Naeini, K. Hsu, D. Braithwaite, and S. Sorooshian, 2021b: PERSIANN-CCS-CDR, a 3-hourly 0.04° global precipitation climate data record for heavy precipitation studies. *Scientific Data 2021 8:1*, **8**, 1–11, https://doi.org/10.1038/s41597-021-00940-9.

Saemian, P., and Coauthors, 2021: Comprehensive evaluation of precipitation datasets over Iran. *Journal of Hydrology*, **603**, 127054, https://doi.org/10.1016/J.JHYDROL.2021.127054.

Schreck, C. J., and J. Molinari, 2011: Tropical Cyclogenesis Associated with Kelvin Waves and the Madden–Julian Oscillation. *Monthly Weather Review*, **139**, 2723–2734, https://doi.org/10.1175/MWR-D-10-05060.1.

Sellars, S., P. Nguyen, W. Chu, X. Gao, K. L. Hsu, and S. Sorooshian, 2013: Computational earth science: Big data transformed into insight. *Eos (United States)*, https://doi.org/10.1002/2013EO320001.

——, S. L., X. Gao, and S. Sorooshian, 2015: An object-oriented approach to investigate impacts of climate oscillations on precipitation: A western United States case study. *Journal of Hydrometeorology*, https://doi.org/10.1175/JHM-D-14-0101.1.

——, S. L., B. Kawzenuk, P. Nguyen, F. M. Ralph, and S. Sorooshian, 2017: Genesis, Pathways, and Terminations of Intense Global Water Vapor Transport in Association with Large-Scale Climate Patterns. *Geophysical Research Letters*, **44**, 12,465-12,475, https://doi.org/10.1002/2017GL075495.

Seneviratne, S., and Coauthors, 2012: Changes in climate extremes and their impacts on the natural physical environment. 109–230, https://doi.org/10.7916/D8-6NBT-S431.

Shearer, E., V. Afzali, G. Uc, I. Phu, N. Uc, I. Kuo-Lin, H. Uc, and I. S. Sorooshian, 2022: Unveiling four decades of intensifying precipitation from tropical cyclones using satellite measurements. https://doi.org/10.21203/rs.3.rs-1233369/v1.

——, E. J., P. Nguyen, S. L. Sellars, B. Analui, B. Kawzenuk, K. lin Hsu, and S. Sorooshian, 2020: Examination of Global Midlatitude Atmospheric River Lifecycles Using an Object-Oriented Methodology. *Journal of Geophysical Research: Atmospheres*, **125**, e2020JD033425-e2020JD033425, https://doi.org/10.1029/2020JD033425.

Shields, C. A., and Coauthors, 2018: Atmospheric River Tracking Method Intercomparison Project (ARTMIP): Project goals and experimental design. *Geoscientific Model Development*, https://doi.org/10.5194/gmd-11-2455-2018.

Skok, G., J. Bacmeister, and J. Tribbia, 2013: Analysis of Tropical Cyclone Precipitation Using an Object-Based Algorithm. *Journal of Climate*, **26**, 2563–2579, https://doi.org/10.1175/JCLI-D-12-00135.1.

Sorooshian, S., K. L. Hsu, X. Gao, H. v. Gupta, B. Imam, and D. Braithwaite, 2000: Evaluation of PERSIANN system satellite-based estimates of tropical rainfall. *Bull Am Meteorol Soc*, https://doi.org/10.1175/1520-0477(2000)081<2035:EOPSSE>2.3.CO;2.

Thapa, K., T. A. Endreny, and C. R. Ferguson, 2018: Atmospheric Rivers Carry Nonmonsoon Extreme Precipitation Into Nepal. *Journal of Geophysical Research: Atmospheres*, **123**, 5901–5912, https://doi.org/10.1029/2017JD027626.

Touma, D., S. Stevenson, S. J. Camargo, D. E. Horton, and N. S. Diffenbaugh, 2019: Variations in the Intensity and Spatial Extent of Tropical Cyclone Precipitation. *Geophysical Research Letters*, **46**, 13992–14002, https://doi.org/10.1029/2019GL083452.

Traxl, D., N. Boers, A. Rheinwalt, and B. Bookhagen, 2021: The role of cyclonic activity in tropical temperature-rainfall scaling. *Nature Communications 2021 12:1*, **12**, 1–9, https://doi.org/10.1038/s41467-021-27111-z.

Trenberth, K. E., 2011: Changes in precipitation with climate change. *Climate Research*, **47**, 123–138, https://doi.org/10.3354/CR00953.

Viale, M., R. Valenzuela, R. D. Garreaud, and F. M. Ralph, 2018: Impacts of atmospheric rivers on precipitation in Southern South America. *Journal of Hydrometeorology*, **19**, 1671–1687, https://doi.org/10.1175/JHM-D-18-0006.1.

Villarini, G., D. A. Lavers, E. Scoccimarro, M. Zhao, M. F. Wehner, G. A. Vecchi, T. R. Knutson, and K. A. Reed, 2014: Sensitivity of Tropical Cyclone Rainfall to Idealized Global-Scale Forcings. *Journal of Climate*, **27**, 4622–4641, https://doi.org/10.1175/JCLI-D-13-00780.1.

Walsh, K. J. E., S. J. Camargo, T. R. Knutson, J. Kossin, T.-C. Lee, H. Murakami, and C. Patricola, 2019: Tropical cyclones and climate change. *Tropical Cyclone Research and Review*, **8**, 240–250, https://doi.org/10.1016/J.TCRR.2020.01.004.

Weber, H. C., C. C. F. Lok, N. E. Davidson, and Y. Xiao, 2014: Objective Estimation of the Radius of the Outermost Closed Isobar in Tropical Cyclones. *Tropical Cyclone Research and Review*, **3**, 1–21, https://doi.org/10.6057/2014TCRR01.01.

Weinkle, J., R. Maue, and R. Pielke, 2012: Historical Global Tropical Cyclone Landfalls. *Journal of Climate*, **25**, 4729–4735, https://doi.org/10.1175/JCLI-D-11-00719.1.

Wille, J. D., V. Favier, A. Dufour, I. v. Gorodetskaya, J. Turner, C. Agosta, and F. Codron, 2019: West Antarctic surface melt triggered by atmospheric rivers. *Nature Geoscience*, **12**, 911–916, https://doi.org/10.1038/S41561-019-0460-1.

WorldBank, 2010: The World Bank Annual Report 2010. https://doi.org/10.1596/978-0-8213-8376-6.

Wuebbles, D. J., and Coauthors, 2014: CMIP5 Climate Model Analyses: Climate Extremes in the United States. *Bull Am Meteorol Soc*, **95**, 571–583, https://doi.org/10.1175/BAMS-D-12-00172.1.

——, and Coauthors, 2017: Climate Science Special Report. *Executive Summary of the Climate Science Special Report: Fourth National Climate Assessment*, https://doi.org/10.7930/J0J964J6.

Zhao, C., Y. Lin, F. Wu, Y. Wang, Z. Li, D. Rosenfeld, and Y. Wang, 2018: Enlarging Rainfall Area of Tropical Cyclones by Atmospheric Aerosols. *Geophysical Research Letters*, **45**, 8604–8611, https://doi.org/10.1029/2018GL079427.

Zhou, Y., H. Kim, and B. Guan, 2018: Life Cycle of Atmospheric Rivers: Identification and Climatological Characteristics. *Journal of Geophysical Research: Atmospheres*, **123**, 12,715-12,725, https://doi.org/10.1029/2018JD029180.